Chapter 3

Narrow- and Broad-band imaging of radio galaxies and quasars

3.1 Introduction

Radio galaxies and quasars often show extra-nuclear emission-line gas around them to the extent of tens of kilo parsec. The large scale emission-line gas is distributed in filamentary structures with low filling factors and are often found near the boundaries of radio lobes or adjacent to bright radio features. This emission-line gas provides us some means of studying the interaction of radio jets with the environment. It could also cause depolarization of the radio radiation by forming a Faraday depolarizing medium. In a majority of the cases, these emission-line regions tend to align closely with the radio source axis and are often highly asymmetric (e. g. McCarthy, van Breugel & Kapahi 1991; McCarthy 1993; di Serego Alighieri 1997).

3.1.1 Alignment effect

In 1987, McCarthy et al. (1987) and Chambers et al. (1987) found, in their sample of radio sources, that the optical continua were elongated and closely aligned with the radio source axes. This positional correlation is known by the name "alignment effect", and is significant in radio sources (see McCarthy 1993 for a review) at redshifts of ~ 0.6 or higher. The alignment effect was first noted in some of the 3CR and 4C sources, and has been studied further at both radio and optical wavelengths for 3CR and other radio sources (Best, Longair & Röttgering 1996; 1997; Rush et al. 1997). In the sample of 3CR radio sources observed by Best et al. (1997), most of the sources show highly elongated optical emission aligned with the radio source axis. The smaller radio sources show a string of bright knots of optical emission tightly aligned along the radio axis, while more extended sources contain fewer bright components. The most favoured models of alignment effects are jet induced star formation and scattering of an anisotropic continuum from a central AGN (Tran et al. 1998). According to the star formation model, the passage of radio

jet through the interstellar medium of the galaxy will induce star formation (Rees 1989; Best et al. 1996; van Breugel & Dey 1993). When the radio hotspots pass beyond the interstellar medium, the star formation would cease and these clusters of stars will age. In the scattering model, the nuclear light is scattered by dust or electrons present within the opening angle of the torus (e. g. Tran et al. 1998). Evidence for this mechanism comes from the polarimetric studies showing high polarizations in the extended emission, with the polarization position angle perpendicular to the radio source axis (di Serego Aligheri et al. 1994).

3.1.2 Interaction between radio source and the emission-line gas

There has been evidence in the past for interaction of the radio jets with emission-line gas, which may be ionised by interaction with the radio jet or due to photoionisation by continuum from the AGN (Fosbury 1997; Prieto et al. 1993).

- Radio and optical observations of Minkowski's object (van Breugel et al. 1985a) showed that it is a region with bright optical line and continuum emission and lies in the direction of the radio jet emanating from NGC541. The optical emission is brightest near the edges of the jet, correlates with the absence of polarised radio emission, and is filamentary downstream where the radio jet is deflected and decollimated. These properties of the radio jet suggest that it might be colliding with a relatively dense gas cloud or small irregular galaxy.

- Baum & Heckman (1989a, b) studied a large number of powerful radio sources and tried to address the question on whether the emission-line gas is affected by the radio source dynamics, or vice versa. The emission-line gas tends to lie in the same quadrant as the radio emission. A logical explanation is that radio source contributes to the ionisation via shocks and/or ultraviolet extension of the non-thermal radiation from the central engine. Small radio sources ($D_{radio} < 150h_{75}^{-1}$kpc) which have emission-line gas associated with them show clear morphological distortions in radio structures and lower fractional polarizations at radio frequencies, while large radio sources ($D_{radio} > 150h_{75}^{-1}$kpc) show largely undistorted, normal FRII radio structures and relatively higher fractional radio polarization.

- In a sample of about 12 3CR radio galaxies, Pedelty et al. (1989) have shown that the lobe closer to the nucleus is also the more depolarized lobe. The depolarization and rotation measure distributions of their sources were patchy on the scale of 5 to 50 kpc indicating the presence of an irregular magnetoionic medium on this scale. In five of their eight radio galaxies where optical emission-line gas is seen, the depolarized radio emission and the optical emission-line gas show clear spatial association. This emission-line gas could be acting as the depolarizing medium. The

arm-length ratio of the two radio lobes show significant asymmetries in the sense that the nearer lobe is on the same side where the emission-line gas is more. This is consistent with the hypothesis that the velocities of advancement of the jets are slowed by the presence of the asymmetrically distributed emission-line gas.

- A systematic study by McCarthy et al. (1991) aimed at investigating the role of the distribution of emission-line gas in radio source dynamics, further confirmed that the emission-line gas affects the propagation of radio jets. One important result from their study is that the the closer lobe is on the same side as the brighter emission-line gas. The study also showed that the lobe closer to the nucleus is the brighter one in about 65% of the sources again establishing the correlation between radio source properties and the optical emission-line gas distributions.

- **3C171** This is a high-luminosity FRII type radio galaxy at a redshift of 0.2384, well studied by Heckman, van Breugel & Miley (1984). The radio source morphology shows clear distortion near the emission-line gas. The brighter radio knots are co-spatial with the brighter patches of emission-line gas, and the radio structure is highly distorted in the vicinity of the emission-line gas. The radio emission is depolarized in the regions where the emission-line gas overlaps the radio emission, again establishing that emission-line gas could depolarize the radio radiation.

- **3C275.1** This radio quasar at a redshift of 0.55 shows clear association of its polarization properties with the environment. Optical galaxies are seen in the more depolarized sections, while in the surrounding area the polarization is more uniform. The strongly depolarized southern lobe also shows clear association with emission-line gas, indicating that the depolarization might be caused by the emission-line gas itself (Liu & Pooley 1990).

- **3C277.3** The Hα emission-line images of this radio galaxy clearly demonstrate the interaction of the radio structure with the emission-line gas. The brightest radio features are seen associated with the brightest emission-line gas distribution, the radio emission bends and widens near bright emission-line patches. Moreover, the strongly depolarized region is found spatially associated with the distribution of emission-line gas suggesting again that the radio emission might be depolarized by this gas (van Breugel et al. 1985b).

In the previous Chapter we discussed the Laing-Garrington effect according to which the lobe on the jet side is almost always the less depolarized lobe. This effect is understood as an orientation effect, where the jet-side lobe is pointing towards the observer and has to travel less distance through the depolarizing medium around the parent galaxy than the counter-jet side lobe. While in quasars, the effects of orientation plays a major role,

for the radio galaxies the role of the environment is significant. Our results (cf. Chapter 2) show that the lobe closer to the nucleus is also the more depolarized lobe.

In this Chapter we present the data and results of the narrow- and broad-band imaging of a subset of our sample of sources. The aim of the observation was to study the environments of our sample of sources and correlate with the radio polarization properties and symmetry parameters. The source sample and the observations are presented in the section 3.2, and the results and discussion in section 3.3.

3.2 Sample and observations

The sample of radio galaxies and quasars and the selection criteria are discussed in detail in the previous Chapter. In this Chapter we present the optical observations of a subset of sources from the original sample. Optical narrow-band imaging was done at the redshifted O[II] or O[III] lines with appropriate filters. The broad-band imaging was done using r, i and V filters. For broad-band imaging the r filter of the Thuan & Gunn (1976) system, the i filter of Wade et al. (1979) system and the V filter of the Johnson (1963) system were used. For narrow-band observations, filters centered at 6147, 6520, 6781, 7053, 7531 and 7935 Å with widths of 70 to 80 Å, courtesy of the Lick Observatories, were used. The observations were carried out with the 2.5m Du Pont Telescope at Las Campanas Observatory (LCO), Chile. A 2048 × 2048, thinned and UV flooded, Textronix CCD with 24 μm × 24 μm sized pixels was used. The 2048 × 2048 image was rebinned to derive 1024 × 1024 images. Astrometry was performed using the Digitized Sky Survey images and a pixel scale of about 0.52″ pixel^{-1} was derived. This corresponds to total field size of 532 × 532 arcsec^2 per CCD frame. We have checked our identifications with the finding charts given in McCarthy et al. (1996) and Kapahi et al. (1998a) for radio galaxies and quasars respectively. For CCD image pre-processing, the bias correction was done using the 16 column overscan region of the individual CCD frames. Flatfielding was done for each filter using master dome flats, which were obtained by averaging corresponding individual dome flats. Multiple frames of individual sources were properly aligned and summed to produce the final image. Absolute photometry was not performed on our images as we are interested only in the morphology of the source and in the distribution of the emission-line gas around the source. Instead, each final image was normalised with respect to its mean value near the source. The normalised broad-band continuum images were used to subtract from the normalised narrow-band images to produce the continuum subtracted narrow-band images, except in one source (1023−226) where the narrow- and broad-band filters did not overlap. The data were analysed using the IRAF package provided by National Optical Astronomy Observatory (NOAO).

The properties of the sources and the observing log are presented in Table 3.1 which is arranged as follows. Columns 1, 2 and 3: source name, its optical identification (G for

galaxy and Q for quasar) and redshift; Column 4: filters used in the observations; Column 5: integration time in minutes and Column 6: date of observation. The final images are presented in Figure 3.1.

3.3 Results and Discussion

The narrow- and broad-band images of the radio galaxies and quasars are presented in Figure 8. We now compare the distribution of emission-line gas and galaxies along the radio source axis and correlate these with the symmetry parameters of the radio source. Four galaxies and two quasars have narrow-band observation, and significant extension of emission-line gas is seen in one quasar (1232−249) and possibly in one galaxy (0346−297). In both cases, the extension is in a direction which is within about 30° of the radio source axis, consistent with the alignment effect noted in high-redshift radio galaxies (Chambers et al. 1987; McCarthy et al. 1987). The lobes of both 0346−297 and 1232−249 lie well outside the extent of the emission-line gas, and do not show any significant depolarization between 1.4 and 5 GHz (IC98). We have also looked for evidence of galaxies in the broad-band images for signs of possible interaction with the radio source. In three galaxies (0428−281, 1023−226 and 1358−214), a galaxy is seen within about 5° of the radio axis. The arm-length ratios of all these three galaxies are consistent with slowing down of the jet by possible interaction with the galaxy. In the radio galaxy 3C34 where Best, Longair & Röttgering (1997) have presented evidence of jet-cloud interaction at a distance of 120 kpc from the nucleus of the parent optical galaxy, the primary hotspot on the side of the interaction is closer to the nucleus than the one on the opposite side. This is consistent with the trend seen in our three sources. We comment below briefly on the objects we have observed at optical wavelengths.

Notes on individual sources

0346−297: This galaxy has a very asymmetric radio morphology. Almost the entire radio flux density of the source is due to south-eastern lobe. There is only weak evidence of emission-line gas which is slightly extended to the north-west, roughly in the same direction of the weaker radio lobe. This radio lobe is farther away ($r_\theta \sim 1.7$) from the host galaxy and does not have radio polarization information due to inadequate signal to noise ratio. In the broad-band r image a galaxy is seen about 100 kpc from the center within about 30° of the radio source axis towards the north.

0428−281: There appears to be weak extension of the emission-line gas distribution. An optical galaxy (B) is seen physically connected to the galaxy (A) identified by McCarthy et al. (1996) . However, in the continuum subtracted emission-line image, the galaxy A disappears completely and the galaxy B appears bright. The astrometric position of

Table 3.1: Observation log

Source Name	Id	z	filter	integration (minutes)	Date of Observation
0346−297	G	0.416	7052	70	7th, 8th Mar 1997
			r	13	8th Mar 1997
0428−281	G	0.65	6147	75	7th Mar 1997
			r	10	7th Mar 1997
1023−226	G	0.586	7935	140	5th Mar 1997
			r	26	5th Mar 1997
1052−272	Q	1.103	i	60	8th Mar 1997
			V	40	8th Mar 1997
1126−290	G	0.41	i	20	7th Mar 1997
			V	25	7th Mar 1997
1226−297	Q	0.749	6520	57	5th Mar 1997
			r	20	5th Mar 1997
			V	5	5th Mar 1997
1232−249	Q	0.352	6781	131	8th Mar 1997
			r	20	8th Mar 1997
			V	5	8th Mar 1997
1247−290	Q	0.77	i	20	6th Mar 1997
			V	40	6th Mar 1997
1257−230	Q	1.109	i	40	7th Mar 1997
			V	30	7th Mar 1997
1358−214	G	0.5	7531	80	4th Mar 1997
			i	42	5th Mar 1997
			r	42	5th Mar 1997

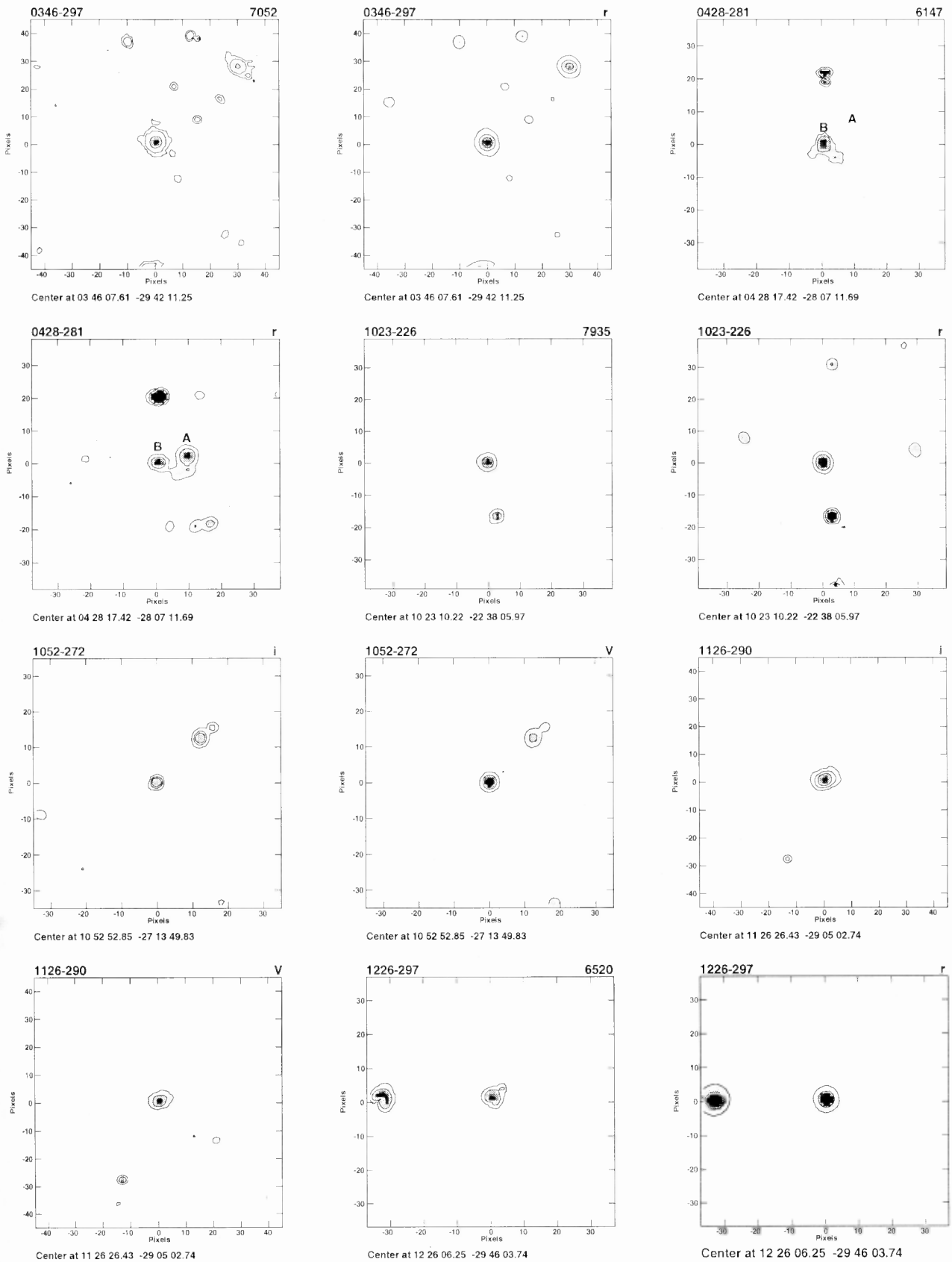

Figure 3.1: Narrow- and broad-band images of radio galaxies and quasars. The x and y axes are in pixels, each pixel corresponds to 0.52 arcsec. The source name is in the top left corner of the image and the observing filter in the top right corner. Each window has a width of 300 kpc. The centers in B1950 co-ordinates are given at the bottom of every image.

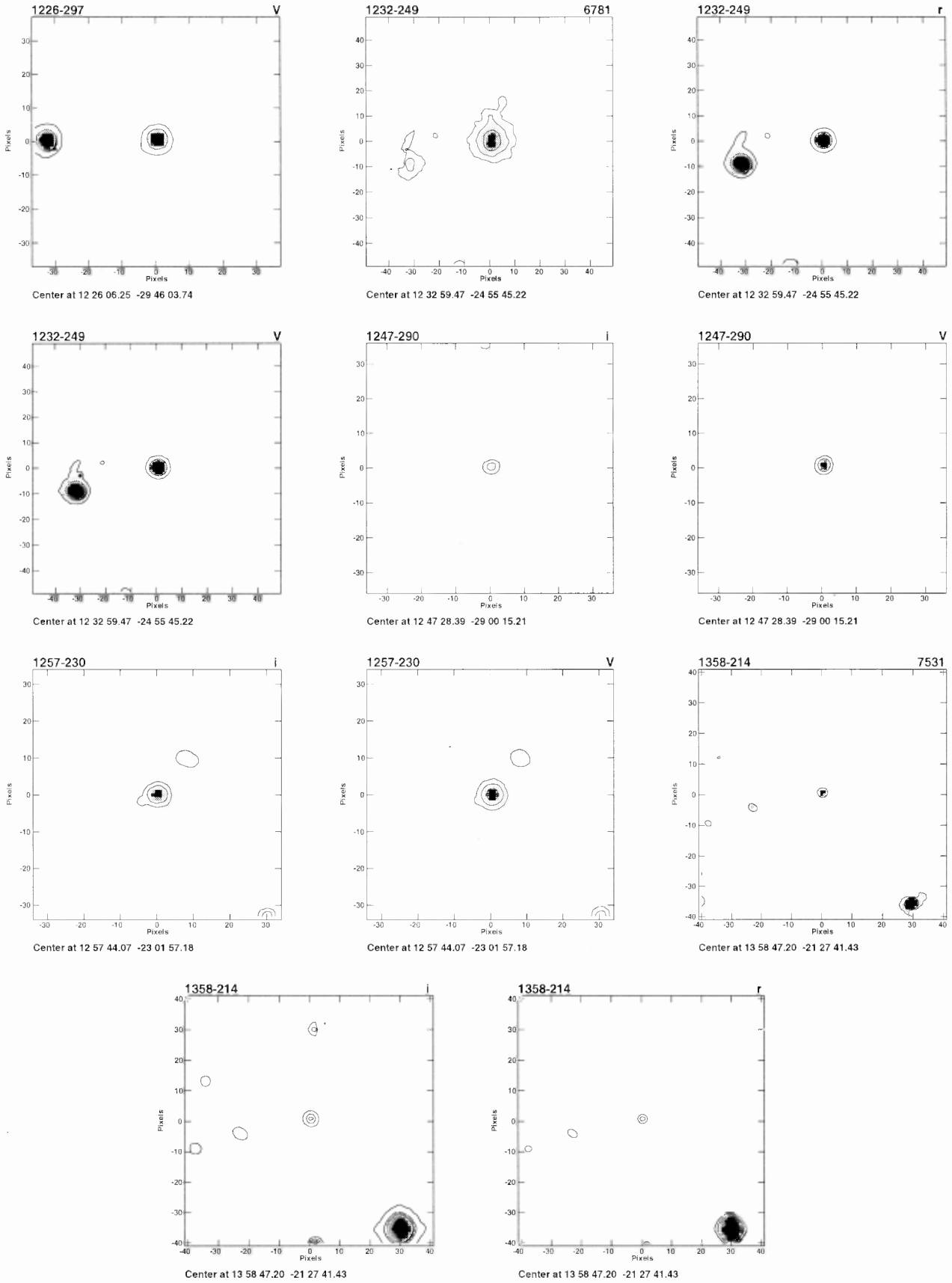

Figure 3.1 : — *continued*

galaxy B is at RA of 04h 28m 17.42s and DEC $-28°$ 07′ 11.″69 (B1950). The position of the possible radio core seen in the 8 GHz image is RA = 04h 28m 17.33s and DEC $-28°$ 07′ 11.″20 (B1950), which is within about 1.″5 of the position of B. If the radio core is confirmed, this is likely to be the correct identification. The galaxy A lies about 40 kpc to west of B along the radio source axis. The radio lobe in this direction is shorter and brighter with the arm-length ratio of 0.75 and brightness ratio of about 1.4. Although the hotspot is about 210 kpc from A, the jet might have slowed down in the past due to interaction with A.

1023−226: The data are affected by a bad pixel column on the source, and normalised narrow-band image is presented. In the broad-band image a faint optical galaxy is seen along the radio axis at a distance of about 110 kpc towards north-west. The arm-length ratio of the lobe on this direction is 0.75 and the brightness ratio is 1.8.

1052−272: Only broad-band imaging was done for this quasar. There are no galaxies close to the radio source axis.

1126−290: Only broad-band imaging was done for this radio galaxy. There are two objects, one of which is within about 20° and other is within about 30° of the radio source axis. The farther one is slightly extended and could be a galaxy. The lobe in this direction is longer and weaker with arm-length ratio of 1.24 and brightness ratio of about 0.4.

1226−297: The emission-line image does not show any significant extension in the present image. In the broad-band r image, there are no galaxies seen close to the radio axis.

1232−249: The emission-line gas in this quasar is elongated towards the south, within an angle of about 30° of the radio source axis. This lobe is closer to the nucleus than the opposite lobe, but is not the brighter one. The arm-length ratio is 0.85 and the brightness ratio is about 0.9. Both the lobes do not show depolarization between 1.4 and 5GHz. Lower radio frequency polarization observations will be useful in understanding the relationship between the emission-line gas distribution and possible depolarization. There are no galaxies seen in the broad-band images along the radio axis.

1247−290: This quasar has only broad-band observations and does not have galaxies close to the radio axis.

1257−230: This quasar also has only broad-band observations and does not show any galaxies close to the radio axis.

1358−214: No significant extended emission line gas is seen. The broad-band i image was affected by bad pixels on the galaxy and therefore continuum subtraction is not done for this galaxy. The i band image is not presented here. There is a galaxy along the radio source axis in the r-band image, at a distance of about 110 kpc towards south-west. The source is reasonably symmetric, has an arm-length ratio of 0.94 and brigtness ratio of about 0.7 for the south-western lobe. This galaxy does not have radio polarization

information.

3.4 Concluding remarks

A significant extension of emission-line gas was seen in one quasar 1232−249 and possibly in one galaxy 0346−297. In both cases the extension is in a direction which is within about 30° from the radio axis, consistent with the alignment effect.

We have identified three candidate jet-galaxy/cloud interactions. In these three radio sources (0428−281, 1023−226 and 1358−214), an external galaxy is seen within about 5° of the radio axis. The arm-length ratios of all these three galaxies are consistent with slowing down of the jet by possible interaction with the galaxy.

In the radio galaxy 3C34 where Best, Longair & Röttgering (1997) have presented evidence of jet-cloud interaction at a distance of 120 kpc from the nucleus of the parent optical galaxy, the primary hotspot on the side of the interaction is closer to the nucleus than the one on the opposite side. This is consistent with the trend seen in our three sources. The lobes of both 0346−297 and 1232−249 lie well outside the extent of the emission-line gas, and do not show any depolarization between 1.4 GHz and 5GHz. For 1358−214, we have polarization information at only 1.4 GHz. It will be useful to observe our sample of sources with greater sensitivity at X-ray, optical and radio wavelengths to probe the environment on these scales.

Chapter 4

Relativistic beaming effects in the spectra of cores and hotspots in radio galaxies and quasars

4.1 Introduction

In the orientation-based unified scheme for radio galaxies and quasars, these objects are believed to be intrinsically similar, but appear to be different because of their different orientations to the line-of-sight. The quasars are oriented close to the line-of-sight, while the radio galaxies lie close to the plane of the sky, the dividing line being about 45°. There has been a reasonable degree of observational evidence in different wave bands in support of such a scheme (Scheuer 1987; Barthel 1989; Antonucci 1993; Urry & Padovani 1995).

In this Chapter we investigate the effects of relativistic beaming in the spectra of cores and hotspots in a matched sample of radio galaxies and quasars, to further test the unified scheme for these objects. We have attempted to determine the spectra of the cores using observations at two widely-spaced L-band frequencies, and at C, X and U bands. These observations represent one of the more extensive studies on the spectra of relatively weak cores in lobe-dominated radio sources. In an earlier study, Athreya et al. (1997) found a high proportion of cores in their sample of high-redshift radio galaxies to have a steep radio spectrum between 4.7 and 8.3 GHz, and identified this with the optically thin part of the core spectrum. They also examined the spectra of core- and lobe-dominated quasars from available data in the literature, and suggested that the galaxy and quasar cores have intrinsically similar radio spectra. Lonsdale, Barthel & Miley (1993) found most of the radio cores in their sample of high-redshift, lobe-dominated quasars to have steep spectra between 5 and 15 GHz, indicating the presence of optically thin components. This is possibly due to the high emitted frequencies corresponding to these sources. We present the spectra of the cores in our sample and examine the effects of relativistic beaming in Section 4.4.

Table 4.1: Observing log

Array Conf.	Obs. band	Obs. Freq. MHz	Band-width MHz	Date of obs.
BnA	L	1365	50	1995 Sep 20
	L	1665	25	
CnB	C	4635	50	1996 Jan 20,31
	C	4935	50	
DnC	U	14965	50	1997 Sep 15, 16
DnC	U	14965	50	1997 Oct 3, 4, 12
BnA	X	8447	25	1997 Feb 3

Relativistic effects in the spectra of hotspots in radio galaxies and quasars selected from the 3CR sample have been examined recently by Dennett-Thorpe et al. (1997, 1999). For the quasars they find that the spectrum of the high surface brightness region is indeed flatter on the jet side, but the spectrum of the low-brightness region is flatter on the side with the longer lobe. They interpret these results in terms of relativistic bulk motion in the high brightness regions, and differential synchrotron ageing in the low-brightness regions. For the FRII galaxies, the spectral asymmetries appear to be uncorrelated with jet sidedness at all brightness levels, but appear to be related to relative lobe volume. In addition, earlier studies have shown that the less depolarized lobe has a flatter radio spectrum (Liu & Pooley 1991), and generally faces the radio jet (Laing 1988; Garrington et al. 1988; Garrington, Conway & Leahy 1991). We examine the effects of relativistic beaming in the spectra of the hotspots in our sample of radio galaxies and quasars using the scaled-array observations at L, C and U bands. These results are presented in Section 4.5. We also show that the hotspot spectra steepen with redshift or radio power and examine whether the shift in rest frequency due to cosmological redshift may account for the observed relationship.

In this Chapter, the sample and the observations are described in Section 4.2, while the observational results on the radio cores are presented in Section 4.3. The observed core prominence, the core spectra and their consistency with the unified scheme are presented in Section 4.4. The consistency of the hotspot spectra with the relativistic beaming effects and the unified scheme, as well as the dependence of hotspot spectra on redshift or luminosity are discussed in Section 4.5. The conclusions are summarised in Section 4.6.

4.2 Source Sample and observations

The sample and the selection criteria are discussed in detail in Chapter 2 reporting the polarization properties of this well-defined sample of radio galaxies and quasars selected

from the Molonglo MRC/1Jy sample (cf. Chapter 2). Briefly, the sample consists of 15 quasars and 27 radio galaxies larger than about an arcminute in size with similar redshift, luminosity and projected linear size distributions. The observations were made with scaled arrays of the Very Large Array (VLA) of the National Radio Astronomy Observatory at 1.4 and 1.7 GHz (L-band), 5 GHz (C-band) and 15 GHz (U-band) with resolutions of $\sim 5''$, while observations at 8 GHz (X-band) have a resolution of $\sim 1''$. At 15 GHz, 14 quasars and 10 radio galaxies were observed, while at 8 GHz only those sources in the RA range 03h to 13h were observed due to scheduling constraints. The observing log is summarized in Table 4.1. All the data were calibrated and analyzed using the NRAO `AIPS` package. The images at X band and U band were corrected for primary beam attenuation. The U-band images have been restored with the same resolutions as the L- and C-band images, which are listed in Table 2.3 of Chapter 2. The images at the X- and U-band are presented in the Appendices 4B and 4C.

4.3 Detection of radio cores

All the quasars have detected radio cores at all wavelengths. In the case of radio galaxies, only two have reliable cores at all wavelengths, but many of them have weak cores in at least one wavelength. Of the 27 radio galaxies, 14 of them have a core detected in at least one wavelength, only 5 of which have a core flux density greater than 1 mJy. These 14 include two possible cores which are weak features seen in only the X-band images close to the positions of the optical galaxies. The peak flux densities of cores have been used to minimise contribution from nearby extended emission, and these values have been estimated using the `AIPS` task `IMFIT`. In the giant source 1025−229, the core flux densities have been estimated by fitting a gaussian to both the core and the nearby jet-like component in the L-, C- and U-band images. All the core flux densities estimated from the Gaussian fits are similar to the values at the pixel of maximum brightness near the optical position. Only those cores which could be clearly identified in the images have been listed in Table 4.2, which is arranged as follows. Column 1: Source name; Column 2: optical identification where Q denotes a quasar and G a radio galaxy; Column 3: redshift of the source; Columns 4 to 9: peak flux densities of the cores at 1365, 1665, 4635, 4935, 8450 and 15000 MHz in units of mJy. In a few cases the core flux density could be significantly over-estimated due to extended diffuse emission in its vicinity. These have been marked with a superscript *d*. Columns 9 and 10: spectral indices between L and C band, and between C and U band, where the spectral index, α, is defined as $S(\nu) \propto \nu^{-\alpha}$. The spectral indices have been estimated using linear least square fits between the bands using the core flux densities at both the frequencies in the L and C bands. Cores with the superscript *d* have not been used. Column 11: N indicates that there is a note on the source in the text, while core? indicates a possible core. The positions of the optical

Table 4.2: Observed and derived parameters of the radio cores

Source Name	Id	z	Flux density of the core						α_L^C	α_C^U	f_c	Notes
			1365 MHz	1665 MHz	4635 MHz	4935 MHz	8450 MHz	15000 MHz				
0017−207	Q	0.545	2.8[d]	2.8	2.2	2.1		1.2	0.25	0.51	0.017	N
0058−229	Q	0.706	4.3[d]	3.8[d]	2.1	2.4		1.0	0.51	0.71	0.020	
0133−266	Q	1.53	14.1	13.2	16.6	16.8			−0.17		0.10	
0148−297	G	0.41	1.9		0.4			2.5			0.00060	N
0428−281	G	0.65			∼0.3	∼0.2	∼0.3				0.00074	N
0437−244	Q	0.84	16.9	15.2	12.8	12.5	10.5	4.4	0.21	0.92	0.089	
0454−220	Q	0.533	190.7	180.5	137.0	137.5	167.4	162.1	0.26	−0.15	0.26	
0551−226	G	0.8					0.4				0.0040	N
0938−205	G	0.371					0.6				0.0058	
0955−283	G	0.8				0.6	1.0				0.0042	
1022−250	G	0.34					∼0.3				0.0039	N core?
1023−226	G	0.586					0.4				0.0050	
1025−229	Q	0.309	11.9	10.0	10.2	10.2	9.9	7.9	0.07	0.22	0.09	
1026−202	G	0.566			0.7	0.7	0.6	0.7			0.0040	
1029−233	G	0.611		0.8	0.5	0.4	0.5		0.56		0.0036	
1052−272	Q	1.103	2.3	2.1	1.8	2.0	1.2	1.2	0.13	0.40	0.0098	
1107−218	G	1.5					∼0.3				0.0023	N core?
1126−290	G	0.41			1.9	1.7	1.4				0.0054	N
1226−297	Q	0.749	1.7	2.3	4.0	3.9	4.6	4.6	−0.61	−0.13	0.029	
1232−249	Q	0.352	17.5	14.7	11.2	10.6	10.0	8.2	0.34	0.25	0.023	
1247−290	Q	0.77	14.2[d]	11.4[d]	2.4	2.1	1.7	1.2	1.50	0.55	0.013	
1257−230	Q	1.109	16.2	16.4	15.4	15.0	10.1	8.1	0.06	0.55	0.055	
1358−214	G	0.5					0.6				0.0074	
2035−203	Q	0.516	34.7	38.1	40.0	38.7		29.7	−0.073	0.25	0.20	
2040−236	Q	0.704	119.1	116.4	91.7	90.3		74.3	0.22	0.18	0.740	
2118−266	G	0.343	27.2	28.6	51.6	51.8		47.5	−0.53	0.074	0.620	
2213−283	Q	0.946	38.3	40.7	54.2	54.1		56.7	−0.27	−0.04	0.19	
2311−222	G	0.434	2.4	1.6	1.9	1.7		1.1	0.11	0.43	0.0077	
2338−290	Q	0.446	30.4	31.9	40.4	40.8		64.5	−0.23	−0.40	0.40	

Notes on individual sources:

0148−297: The core is relatively weak at 4635 MHz; its position is the same as that of the stronger core at 15 GHz, and also consistent with the one seen at 1365 MHz.

0428−281: A weak radio core is detected at both the C bands as well as the X band. The radio positions of the core are the same in all the frequencies; but the core is about 5.″9 from the optical position given by M96.

0551−226: The radio core detected at X band is about 2.″9 from the optical position listed by M96.

1022−250: The possible radio core is about 2.″1 from the position of the optical galaxy given by M96.

1107−218: The possible radio core is about 1.″6 from the position of the optical galaxy given by M96.

1126−290: The positions of the core at both the C bands and at the X band are consistent, but the core is about 12.″4 from the optical position given by M96. The position of the optical galaxy measured from CCD observations of the field is RA: $11^h\ 26^m\ 26.^s434$ and Dec: $-29^\circ\ 05'\ 02.''74$ in B1950 coordinates (see Chapter 3). This is close to the position of the radio core.

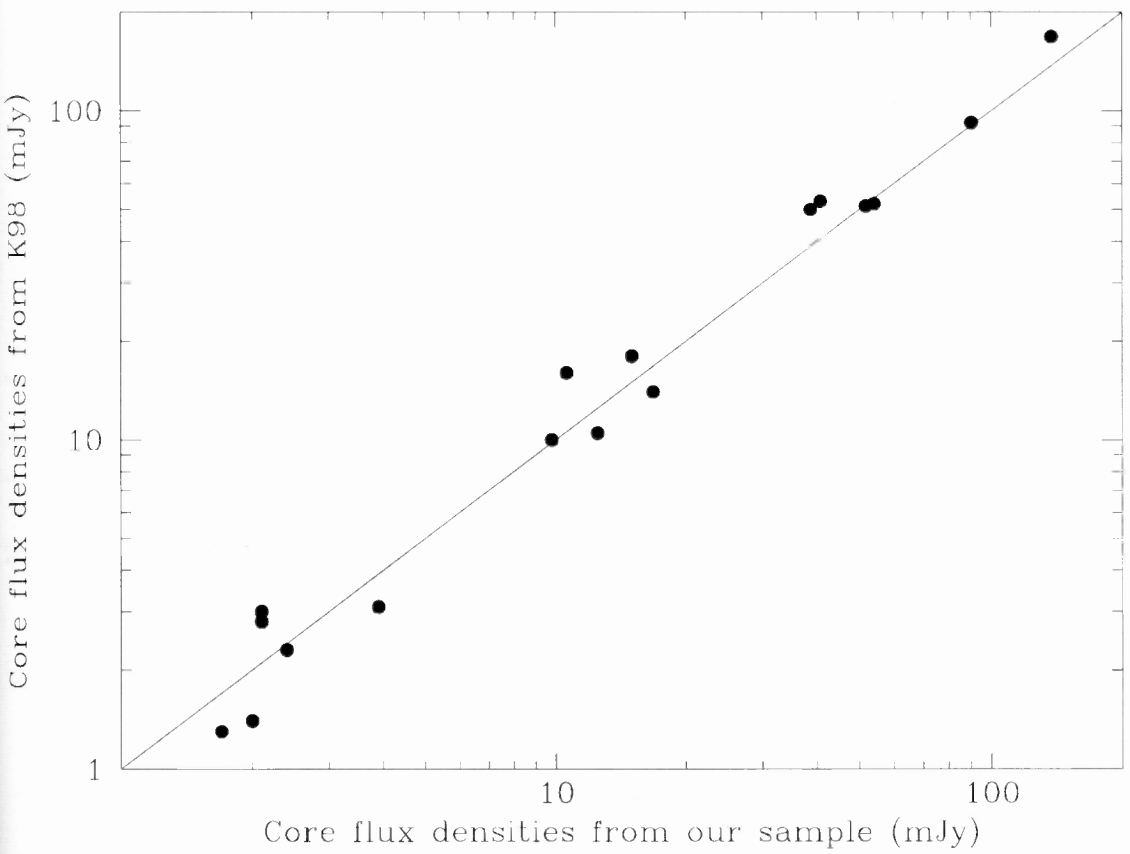

Figure 4.1: Plot of core flux densities at 4.9 GHz from K98 against the values estimated from our observations. Our estimates of core flux densities are from observations with an angular resolution of $\sim 5''$ compared to $\sim 1''$ by K98.

objects have been listed by either McCarthy et al. (1996, hereinafter referred to as M96) if it is a galaxy, or by Kapahi et al. (1998a, hereinafter referred to as K98) if it is a quasar. The typical errors in the optical positions are about $1.''5$ (M96) while for the quasars it is about $0.''5$ (K98). The positions of the new radio cores, which are not listed in K98, are presented in Table 4.3.

4.4 Relativistic beaming in the cores

To examine the consistency of the observations with expectations of the unified scheme, one needs to estimate reliably the flux density of the cores at the different frequencies. Since our observations at all the frequencies except at 8 GHz have been made with coarser angular resolution than is desirable, we have compared our measurements with those of K98, which were made at about 5 GHz with an angular resolution of about $1''$. The data are plotted in Figure 4.1 for all the objects in our sample for which core flux densities have been listed by K98. Since the epochs of the observations are separated by about 5 to 10 yr, there could be differences due to variability of the core flux density. It is, however,

Table 4.3: Positions of radio cores

Source	RA (B1950)	DEC (B1950)
0148−297	01 48 19.679	−29 46 45.00
0428−281	04 28 17.326	−28 07 11.20
0551−226	05 51 17.431	−22 40 18.50
0938−205	09 38 30.873	−20 33 46.60
0955−283	09 55 36.536	−28 23 45.60
1022−250	10 22 57.085	−25 01 08.00
1023−226	10 23 10.267	−22 38 07.00
1026−202	10 26 35.174	−20 12 04.20
1029−233	10 29 12.174	−23 23 56.00
1107−218	11 07 44.986	−21 51 13.40
1126−290	11 26 26.443	−29 05 02.40
1358−214	13 58 47.273	−21 27 40.40

clear from the Figure that the values are consistent over a wide range of flux density. Besides suggesting that the cores might be only weakly variable, this suggests that the effect of the coarser resolution is not significant at 5 GHz. At U band, it is likely to be even less significant, while at the L band we have identified those which are likely to be significantly affected by diffuse emission in the vicinity of the cores.

4.4.1 Core prominence

In the orientation-based unified scheme for radio galaxies and quasars, the quasars are expected to show more prominent cores than radio galaxies due to the effects of relativistic beaming. All quasars have detected cores, compared to about 50% for the radio galaxies. The distributions of f_c, the fraction of emission from the core at an emitted frequency of 8 GHz, for our sample of radio galaxies and quasars is shown in Figure 4.2. The median values of the f_c are about 0.09 ± 0.04 for quasars and less than about 0.0015 ± 0.02 for the radio galaxies. Given the statistical uncertainties due to the small sample, these values are consistent with earlier estimates for the 3CR sample (cf. Saikia & Kulkarni 1994) as well as for a larger sample of Molonglo objects (K98). These values are consistent with the unified scheme for radio galaxies and quasars.

4.4.2 Spectra of cores

Since only two of the galaxies have cores detected at all the observed wavelengths to determine reliably the spectra of the cores (Figure 4.3), we concentrate on the core spectra

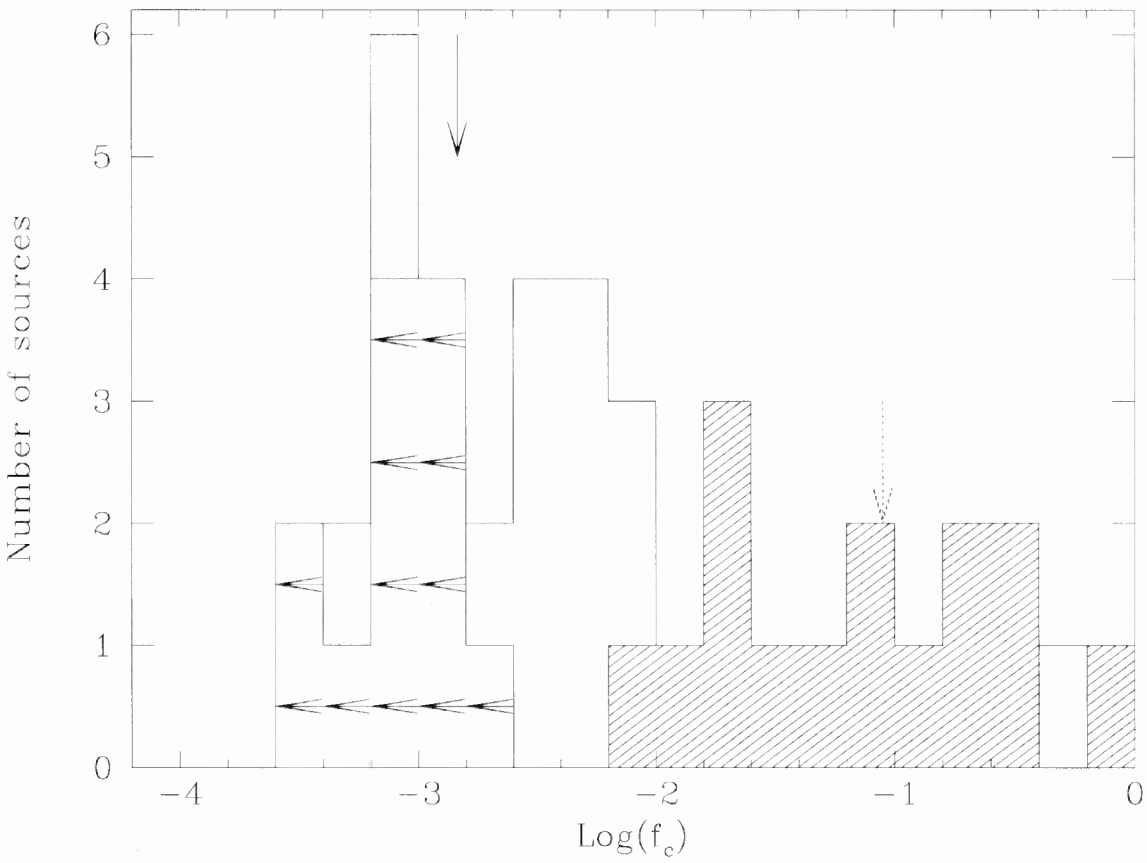

Figure 4.2: Distributions of f_c, the fraction of emission from the core at an emitted frequency of 8 GHz for the Molonglo radio galaxies and quasars in our sample. The quasars are shown hatched, while the upper limits are indicated by horizontal arrows. The median values of f_c for radio galaxies and quasars are shown by vertical solid and dotted arrows respectively.

of the quasars to examine the effects of relativistic beaming. The spectra of all the cores in quasars are presented in Figure 4.4. In both the figures, the error bars correspond to 3% error on absolute flux density calibration and 1σ noise in the image. The spectra have been fitted by either a two- or three-degree polynomial, and in one source, 0454−220, by a straight line and a two-degree polynomial. The spectra are usually complex. The steep low-frequency spectra in the quasars 0058−229 and 1247−290 are possibly due to contributions from more extended emission near the core. The core in 1226−297 is a candidate GPS source (cf. O'Dea 1998) with a turnover frequency around 15 GHz, but higher frequency measurements would be required to confirm this.

In the observed spectra of the cores, the rest frequency in the frame of the quasar will appear shifted due to both cosmological redshift and Doppler shift due to relativistic beaming of the nuclear or core emission. The rest frequency will be shifted by an amount $\delta/(1+z)$ where $\delta = [\gamma(1-\beta\cos\theta)]^{-1}$ is the Doppler factor, z the redshift of the source, γ the Lorentz factor, $\beta = v/c$, and θ is the angle of inclination of the jet or source axis to the line-of-sight. For fixed observed frequencies, ν_1 and ν_2, the spectrum will

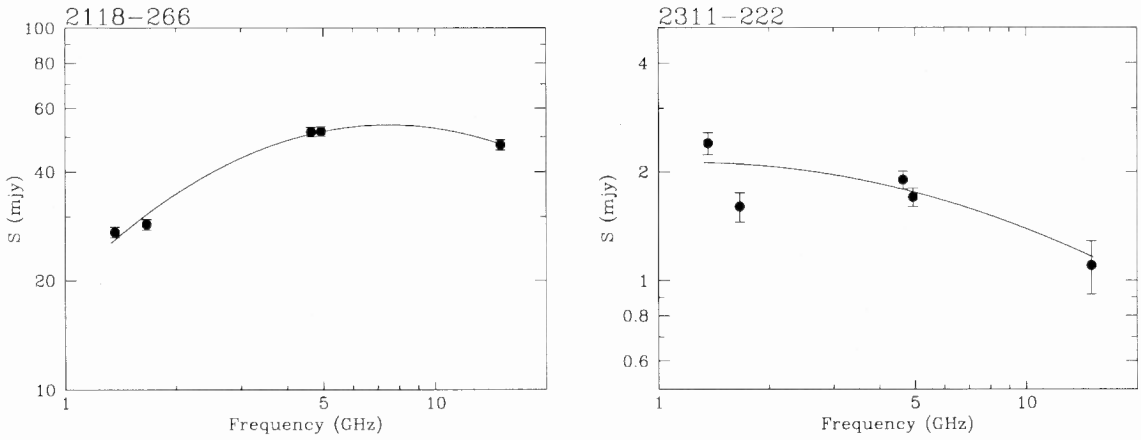

Figure 4.3: Observed spectra of two radio galaxy cores. The X-axis represents the frequency in GHz, while the Y-axis represents the flux density in mJy. The source names are given in the top-left corner of each spectrum. The details of the fits are described in the text.

be blue shifted for quasars, and in case of radio galaxies it will be generally redshifted. Assuming a Lorentz factor of 5, the Doppler factor δ for inclination angles of 15°, 30° and 60°, which correspond roughly to orientations of core-dominated quasars (CDQs), lobe-dominated quasars (LDQs) and radio galaxies, are 3.7, 1.3 and 0.4 respectively. Since we have determined the spectra of only 2 cores in radio galaxies, we concentrate on the quasars and compare their spectra with a sample of core-dominated quasars which have been observed at a single epoch by Saikia et al. (1998). The two samples have similar redshift distributions and have similar extended radio luminosity within a factor of ∼2. We present the distributions of spectral index between 1.4 and 5 GHz (α_C^L) and that between 5 and 15 GHz (α_U^C) for both the samples of LDQs and CDQs in Figure 4.5. These show that both α_C^L and α_U^C for CDQs are flatter compared to the corresponding values of LDQs, and the effect is more prominent in the high-frequency spectral index value (α_U^C). The median values of the two-point spectral index between 1.4 and 5 GHz and that between 5 and 15 GHz for LDQs are 0.13 ±0.069 and 0.25 ±0.085 respectively, while the corresponding values for the CDQs are −0.085 ± 0.073 and −0.073 ± 0.068 respectively. A Kolmogorov-Smirnov test shows that the distributions of α_U^C for LDQs and CDQs are different at $> 99\%$ significance level, while that of α_C^L are different at about 80% significance level. These trends are consistent with the unified scheme since the spectra of CDQs will be blue shifted by a larger amount than LDQs due to relativistic beaming. The trend is more prominent at the higher frequency, possibly due to often being closer to the optically thin region of the synchrotron spectrum.

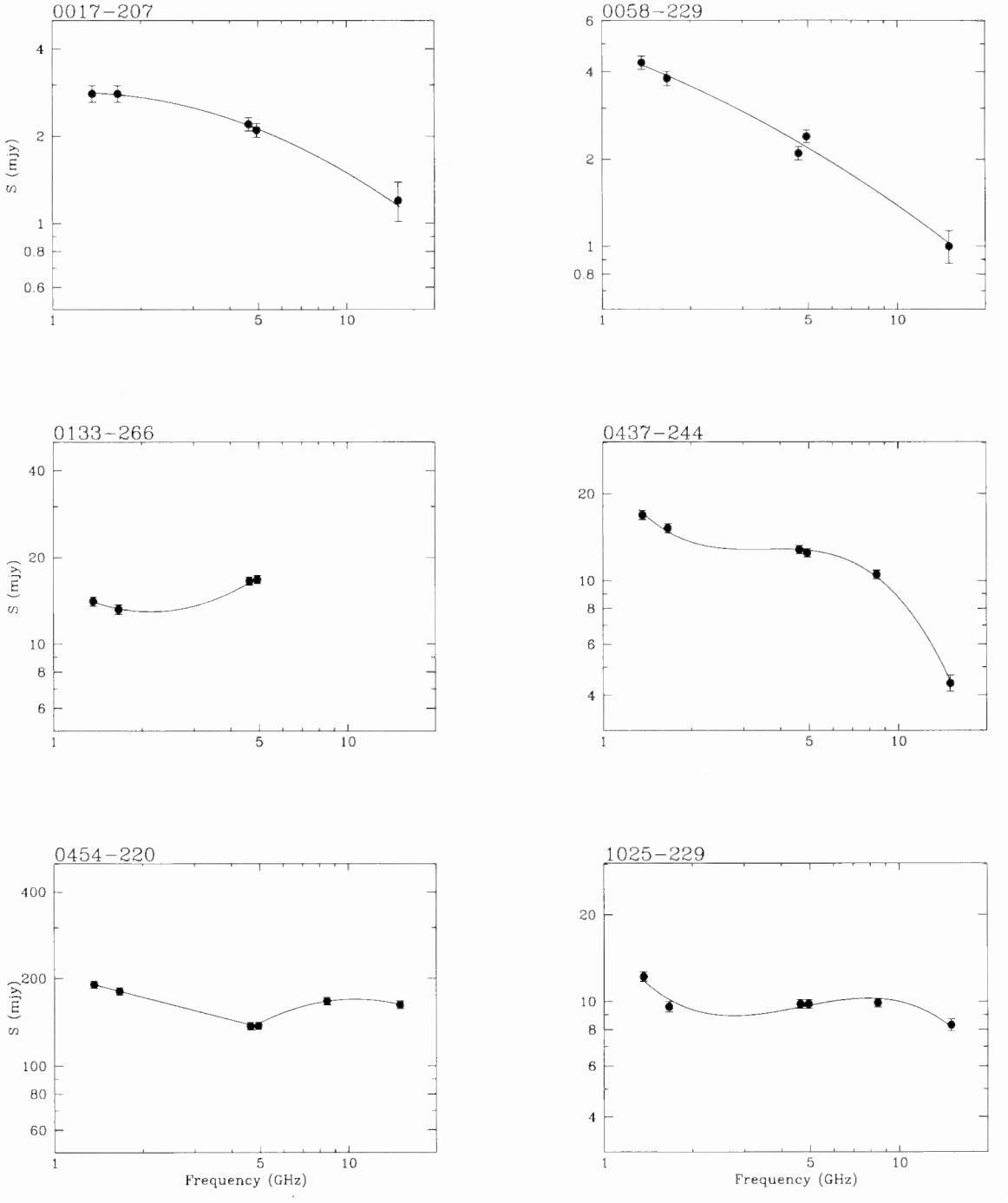

Figure 4.4: Observed radio spectra of quasar cores. The X-axis represents the frequency in GHz, while the Y-axis represents the flux density in mJy. The source names are given in the top-left corner of each spectrum. The details of the fits are described in the text.

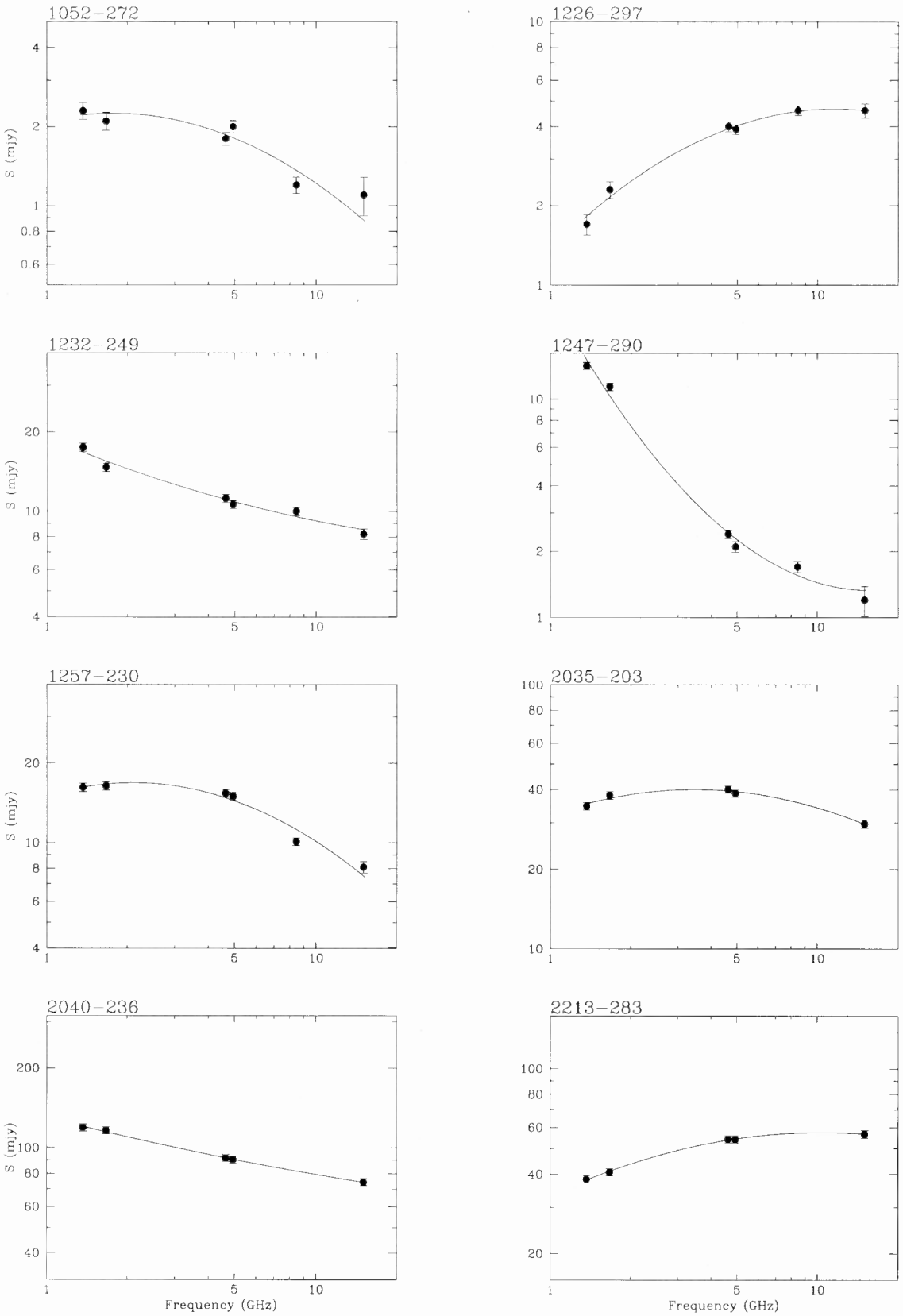

Figure 4.4 — *continued*

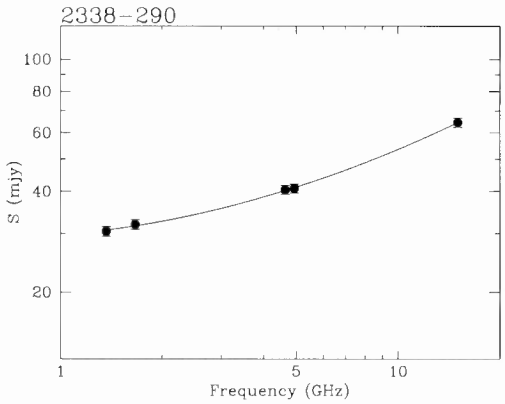

Figure 4.4 — *continued*

4.5 Relativistic motion in the hotspots

Estimates of hotspot advance speeds made from attributing arm-length asymmetries to geometrical projection and light-travel time effects range from about 0.2−0.5c (e.g. Longair & Riley 1979; Banhatti 1980; Best et al. 1995). Tighter constraints have been placed by Scheuer (1995) by noting that the approaching side can be identified in sources with radio jets (cf. Saikia 1981). He estimates an upper limit of ∼0.15c. The properties of highly asymmetric or completely one-sided radio sources indicate hotspot advance speeds in the range of ∼0.2−0.8c (Saikia et al. 1990). Proper motion studies of hotspots in compact VLBI-scale double radio sources yield values from about 0.05-0.5c (cf. O'Dea 1998).

4.5.1 Effects of relativistic motion in hotspot spectra

Assuming that the hotspots are advancing at mildly relativistic speeds, the observed spectral indices of the oppositely directed hotspots might appear to be different due to relativistic motion. If the hotspot spectra steepen towards higher frequencies, the approaching hotspot should exhibit a flatter spectrum over a fixed observed frequency range compared to the receding one due to relativistic Doppler effects. If the spectra are straight, any observed difference will reflect intrinsic differences in their spectra.

In the unified scheme for radio galaxies and quasars, the latter should exhibit a larger difference in the spectral indices of the hotspots on opposite sides due to smaller angles of inclination to the line-of-sight. Assuming a canonical spectrum for the hotspot, one might also be able to estimate the hotspot advance speeds for a sample of sources from the observed difference in hotspot spectral indices. For sources with detected radio jets, one can identify the approaching and receding hotspot. However, since we do not have

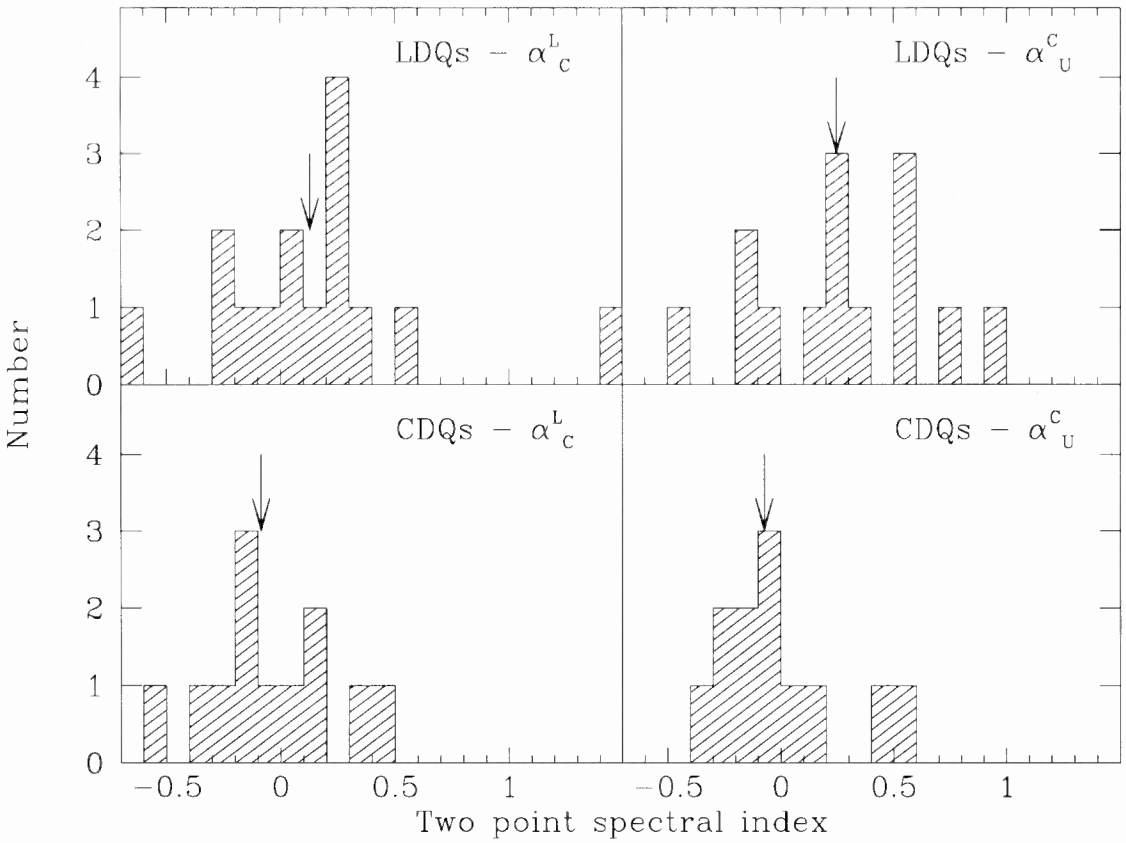

Figure 4.5: Comparison of the two-point spectral indices of lobe-dominated (LDQ) and core-dominated quasars (CDQ). The distributions of the spectral index between the L and C bands and between the C and U bands are shown in the left and right panels respectively. The median values of each distribution are shown by arrows.

detected radio jets in almost all the sources in our sample, we attempt such a study by examining the absolute difference in the hotspot spectral indices of the oppositely directed hotspots for the radio galaxies and quasars. In our study, we have defined the hotspot as the peak pixel in each lobe having surface brightness at least 10 times the weakest reliable flux density level. The number of sources with reliable hotspot flux densities at U band are small. Therefore we concentrate on the L- and C-band observations, but check for consistency with the U-band observations. The Table of hotspot spectral indices and the hotspot spectra are presented in Appendix 4A.

Our samples of radio galaxies and quasars are of similar redshift and luminosity, and therefore the effects of cosmological redshift are similar. The distributions of the absolute difference in the hotspot spectral index $\mid \Delta\alpha \mid$ between 1.4 and 5GHz is shown in Figure 4.6. There is a clear tendency for the quasars to show a larger spectral index difference than radio galaxies. The median values of $\mid \Delta\alpha \mid$ are about 0.055 ± 0.0072 and 0.12 ± 0.015 for the radio galaxies and quasars respectively. A Kolmogorov-Smirnov test shows that the distributions are different at $> 99\%$ significance level. The corresponding values for the spectral indices between C- and U-bands are 0.10 ± 0.015 and 0.19 ± 0.07 for the radio

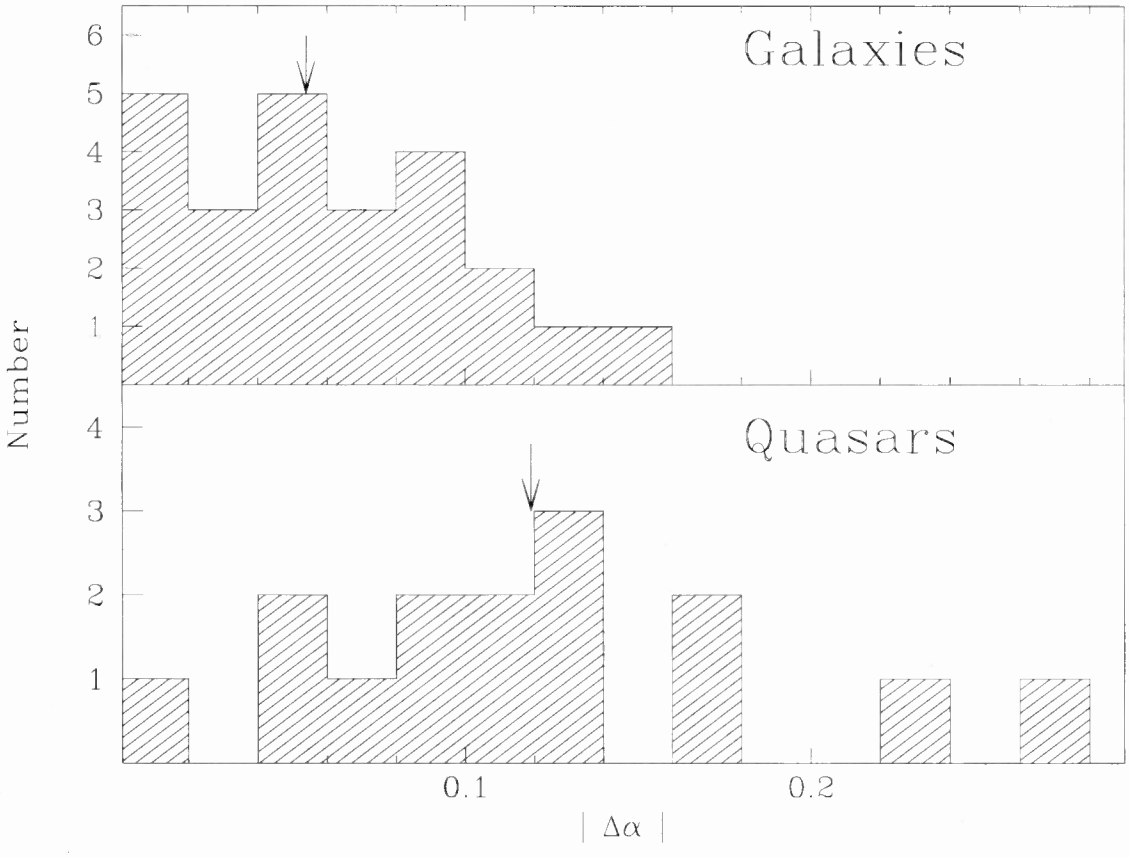

Figure 4.6: The distributions of the absolute difference in the hotspot spectral index $|\ \Delta\alpha\ |$ between 1.4 and 5GHz for the radio galaxies and quasars. The arrows indicate the median values.

galaxies and quasars, again consistent with the trend expected in the unified scheme.

To understand the above difference in terms of relativistic beaming, we have constructed a theoretical hotspot spectra with a curvature of 0.2 in the spectral index between 0.408, 1.4, 5 and 15 GHz. There has been evidence in the past for curvature in the hotspot spectra. For example, Carilli et al. (1991) observed Cygnus A with an angular resolution of about 4.″5 over a large frequency range and find evidence of spectral curvature in the hotspots. Wright, Chernin & Forster (1997) observed the hotspots in Cygnus A with an angular resolution of about 0.″4 and also find evidence of spectral steepening. (See also Section 4.5.2 of this Chapter). The flatter spectra of the hotspots on the jet side can be better explained if the intrinsic spectra is curved downwards towards higher frequencies (Dennett-Thorpe at al. 1997, 1999). Assuming the above spectrum and an angle of 30-40° for quasars and 60-70° for radio galaxies, a hotspot advance speed of ~0.2-0.5c is required to produce the difference. The hotspot advance speed can be less if we assume more curvature in the intrinsic spectra of the hotspots.

If the sources are intrinsically symmetric and the effects of evolution of individual components with age are not dominant, one would expect the approaching hotspot, which

has a flatter spectral index, to be farther from the nucleus and also brighter. However, we have shown in our earlier Chapter that most of these sources appear to be evolving in an asymmetric environment. Nevertheless, for quasars where the effects of orientation are likely to be more significant, we do find a weak trend for the flatter hotspot to be on the longer side. This is true for 9 of the 14 quasars when one considers the spectral index between the L and C bands, and 7 of the 8 quasars for hotspot spectral indices between the C and U bands. The galaxies do not show any trend. We have also examined the relationship of the hotspot spectral indices with hotspot brightness ratio, but do not find any trend possibly due to the effects of environment as well as evolution of the individual components with age.

4.5.2 Spectral index - redshift/luminosity relationship

We have examined the spectral index - redshift/luminosity relationship for our sample using the spectra of the hotspots. There is a significant correlation of the spectral indices between 1.4 and 5 GHz, as well as between 5 and 15 GHz with redshift, the relationship being steeper for the higher frequency spectral index (Figure 4.7). A Spearman rank correlation test shows the relationship to be significant at a level >99 per cent. Since our sources are from a flux-density limited sample, redshift and luminosity are strongly correlated and we cannot distinguish between a dependence on either luminosity or redshift. Linear least-squares fits to the data show the slopes to be 0.30±0.06 and 0.73±0.13 respectively for the low- and high-frequency spectral indices. We have examined the relationship separately for the galaxies and quasars and find that their slopes are similar. Steepening in the hotspot spectra towards higher frequencies, due to radiative losses can, in principle, cause such a relationship since the emitted frequency will be higher for the higher redshift and hence more luminous objects. Inverse-Compton losses would also be important at higher redshifts. In a flux density limited sample, increased magnetic field for the more luminous objects will also increase the synchrotron emissivity, leading to an increase in the rate at which spectral steepening occurs (cf. Laing & Peacock 1980; Gopal-Krishna & Wiita 1990; Krolik & Chen 1991; Blundell, Rawlings & Willott 1999).

The spectral index−redshift plots (Figure 4.7), show that the spectral index increases with z, upto z∼1. For higher redshifts the plot of α_L^C with z, appears to be relatively flat while there are very few points in the α_C^U−z plot beyond z=1. This flattening is consistent with earlier findings by Gopal-Krishna (1988) and van Breugel & McCarthy (1989). In our sample of sources, there is a trend for the high-frequency spectra to be steeper than the low-frequency ones as one goes toward higher redshifts upto z∼1 (Figure 4.8). Beyond a redshift of 1, the relationship needs to be investigated further by getting more reliable estimates of hotspot flux density at U-band for a larger number of sources. This could, in principle, constrain models and help clarify our understanding of the α-z relationship.

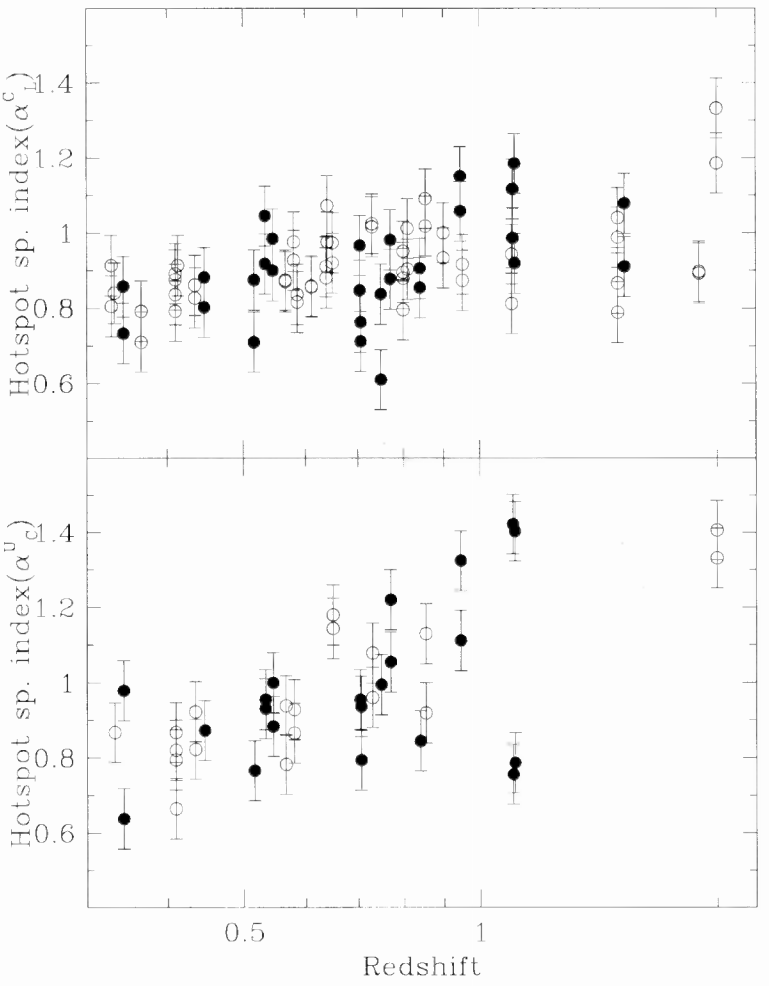

Figure 4.7: Plot of hotspot spectral index against the source redshift. The Y-axis represents the hotspot spectral index between 1.4 and 5GHz (upper panel) and between 5 and 15 GHz (lower panel). Filled and open circles represent quasars and radio galaxies respectively.

Considering all the objects with z<1, and dividing them into two equal groups in redshift the median values of $\alpha_C^U - \alpha_L^C$ are about 0 and 0.06. Although we have plotted the observed spectral indices rather the ones in the rest frame of the source, the median redshift of the objects with z<1 is about 0.6, so that the emitted frequencies for the low-frequency spectral index is about 2.2 and 7.8 GHz. The median values of α_L^C increase from about 0.8 to 1 as the redshift increases from about 0.3 to 1. This range is larger than the observed degree of spectral curvature, indicating that the correlation is not merely due to K-correction factors alone. This is consistent with earlier suggestions (cf. Lacy et al. 1993; van Breugel & McCarthy 1989).

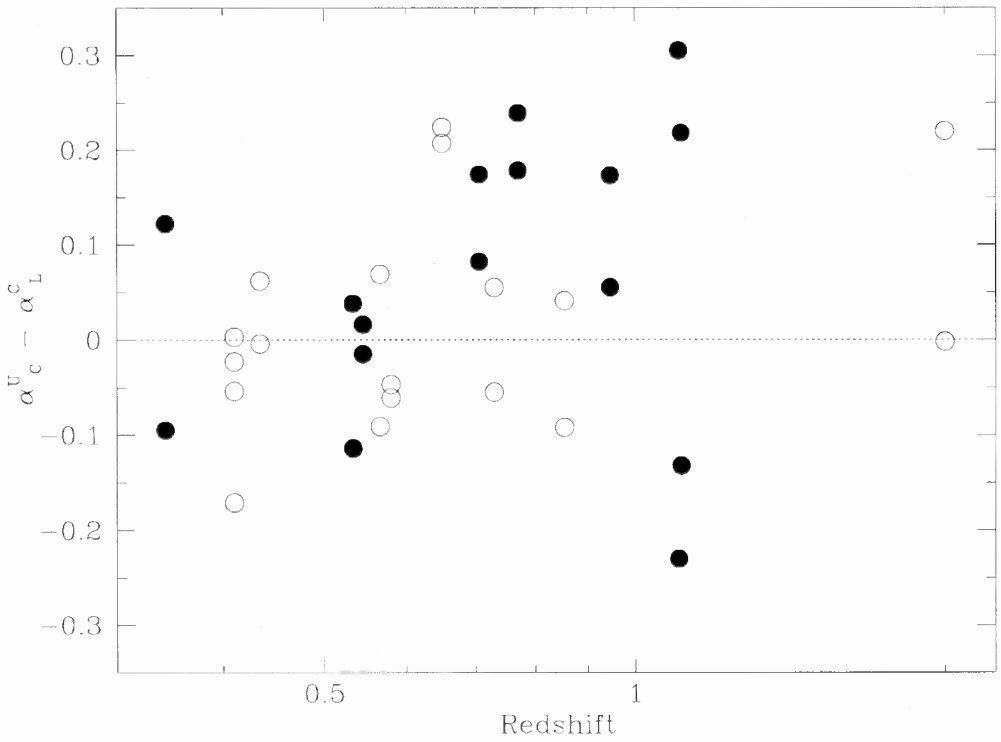

Figure 4.8: Plot of the difference of hotspot spectral index between 5 and 15GHz and that between 1.4 and 5GHz against the source redshift. Filled and open circles represent quasars and radio galaxies respectively.

4.6 Concluding remarks

We have studied multi-frequency radio spectra of cores and hotspots of a matched sample of radio galaxies and quasars. A comparison of the spectral indices of the cores of lobe-dominated and core-dominated quasars shows that the high-frequency spectral index of these two classes are significantly different. The difference can be understood in terms of Doppler effects and are consistent with the basic ideas of the unified scheme for radio galaxies and quasars.

The difference in the spectral indices of the hotspots on opposite sides of the nucleus is larger for quasars compared to radio galaxies, the median values of the difference being about 0.12 and 0.06 respectively. This difference could also be understood in terms of mild relativistic beaming of the hotspots. The hotspots have a curved radio spectrum steepening towards higher frequencies, possibly due to radiative losses. The difference is consistent with the unified scheme for radio galaxies and quasars and yields an estimate of about 0.2 - 0.5c for the velocity of advancement of the hotspots.

The well-known strong correlation between spectral index and redshift/luminosity is also seen in our sample when one considers the hotspot spectral indices. There is some evidence of a flattening of this relationship beyond z$\sim$1, consistent with earlier studies.

Examining the low- and high-frequency spectral indices of the hotspots in our sample, the observed correlation cannot be due to the effects of K-correction alone. The difference in the low- and high-frequency spectral indices of the hotspots needs to be determined reliably for a larger number of high-redshift (z>1) objects to clarify our understanding of the observed $\alpha-$z relationship.

Appendices:

4A. Hotspot Spectra

In this section we present the hotspot spectra and their spectral indices. A two degree polynomial was fitted to the hotspot spectra. The two-point hotspot spectral indices were determined from linear least-square fits to the two L-band and two C-band points for the spectral indices between L and C bands, and to the two C-band and U-band points for spectral indices between C and U bands. The typical errors in the spectran indices are $\sim$ 0.08. These values are presented in the Table 4A.1, which is arranged as follows. Column 1: Source name, with letters N, S, E and W denoting Northern, Southern, Eastern and Western components; Column 2: redshift; Column 3 : spectral index between L- and C-bands and Column 4: spectral index between C- and U-bands. The hospot spectra is presented in Figure 4A. 1. The X- and U-band images are presented in Figures 4B.1 and 4C.1 respectively.

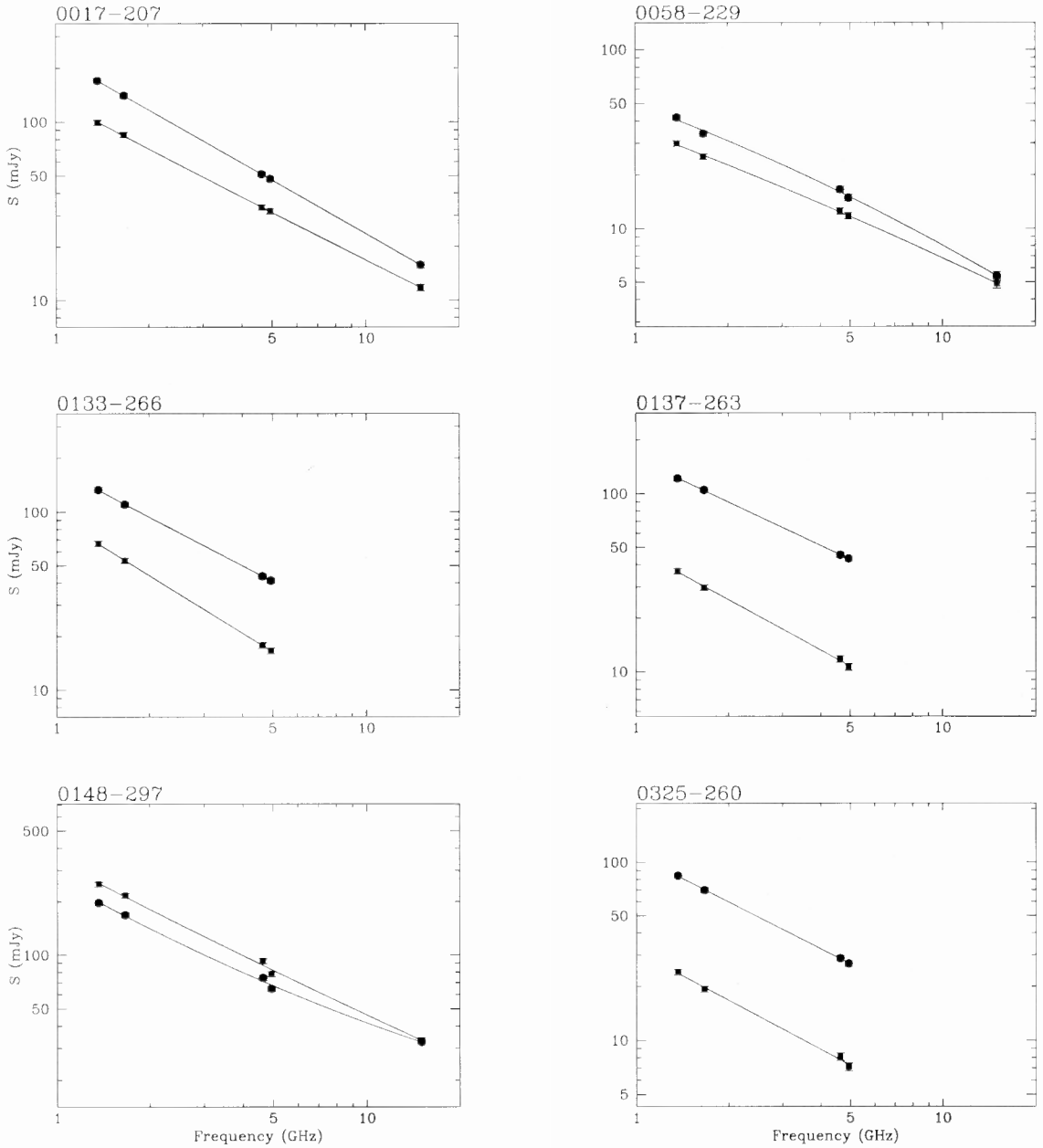

Figure 4A.1 Observed spectra of hotspots between 1.4 and 15GHz. The X-axis represents the frequency in GHz, while the Y-axis represents the flux density in mJy. The source names are given on the top left corner of each spectrum. Errors correspond to 3% error on absolute flux density calibration plus noise (1σ).

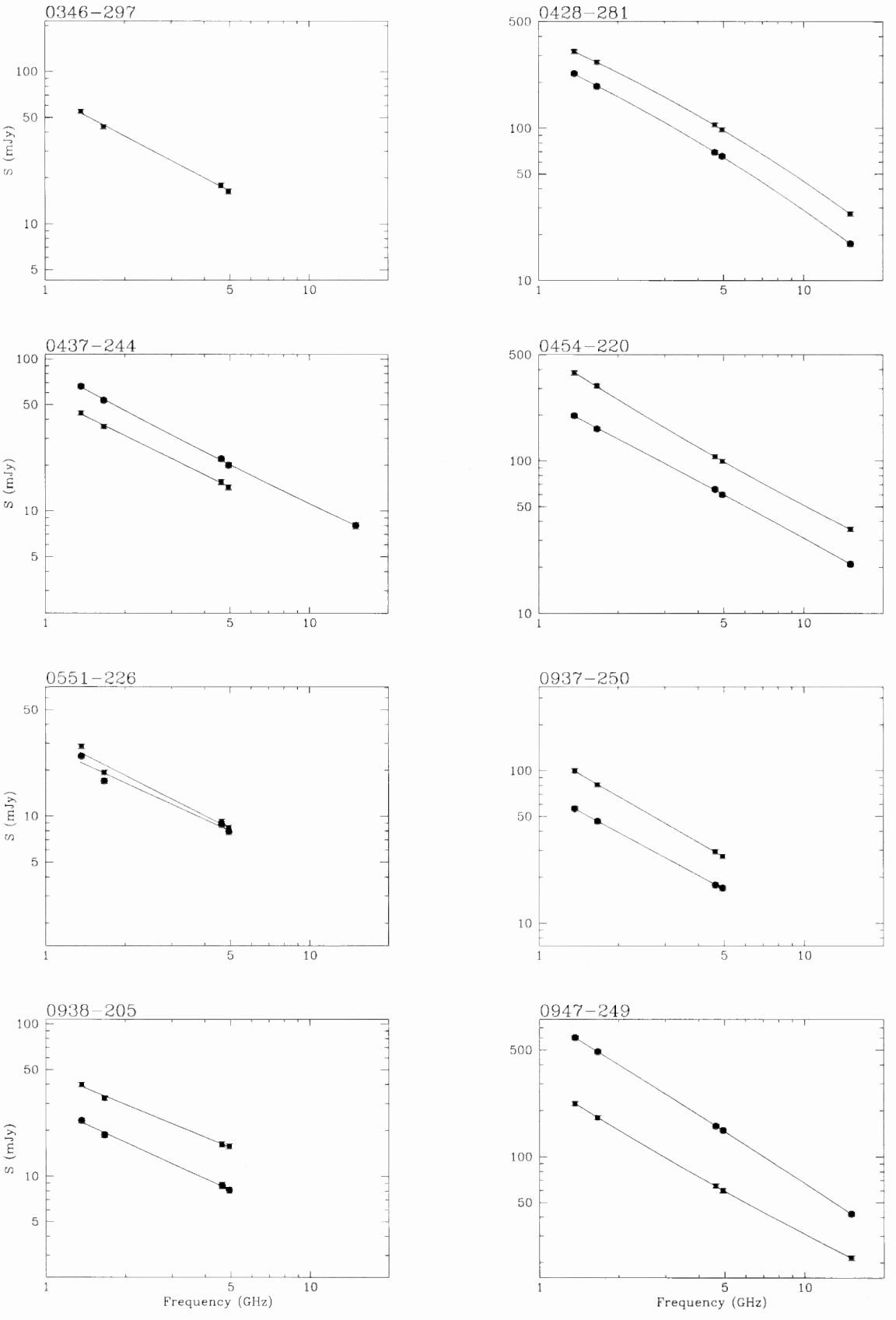

Figure 4A.1 — *continued*

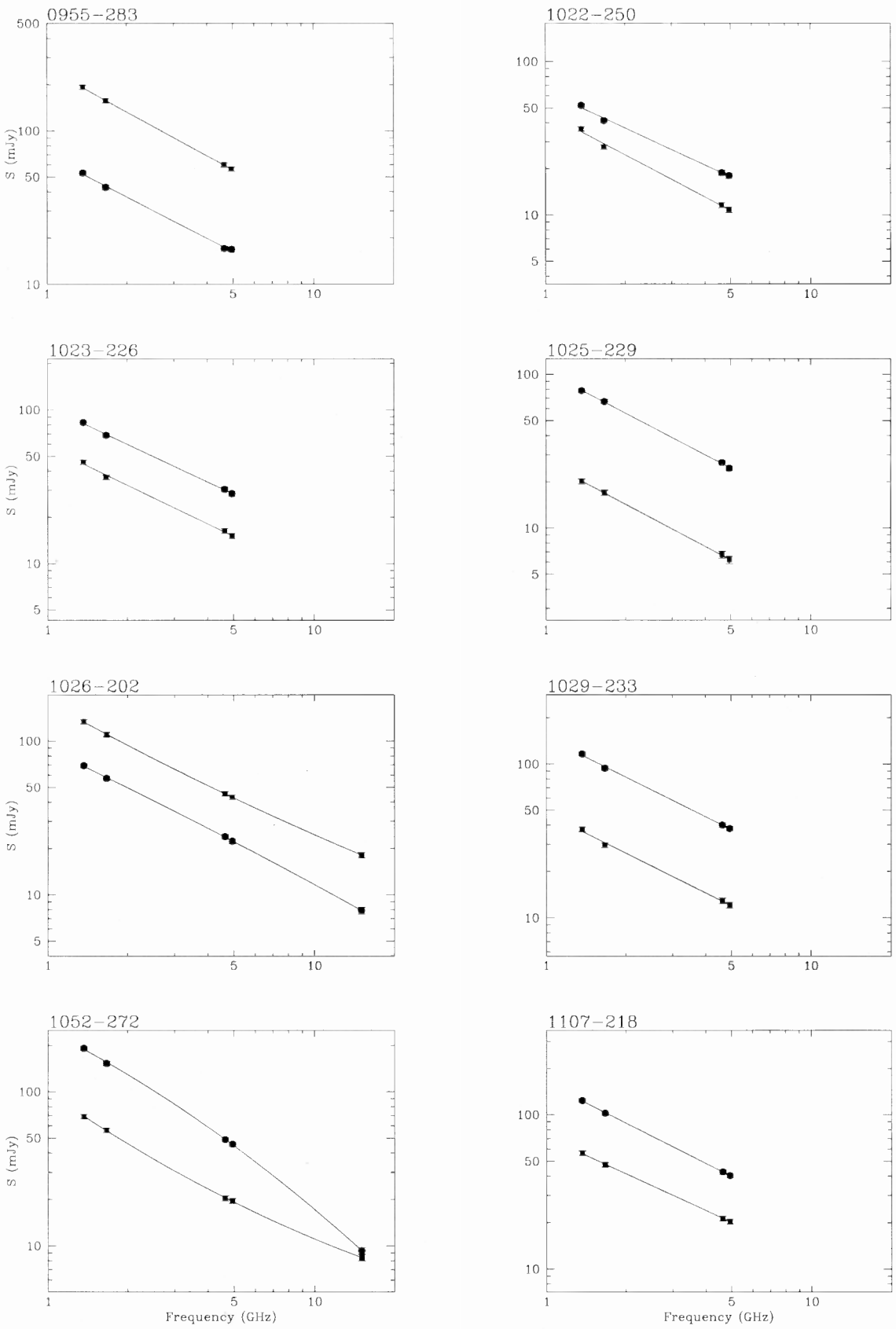

Figure 4A.1 — *continued*

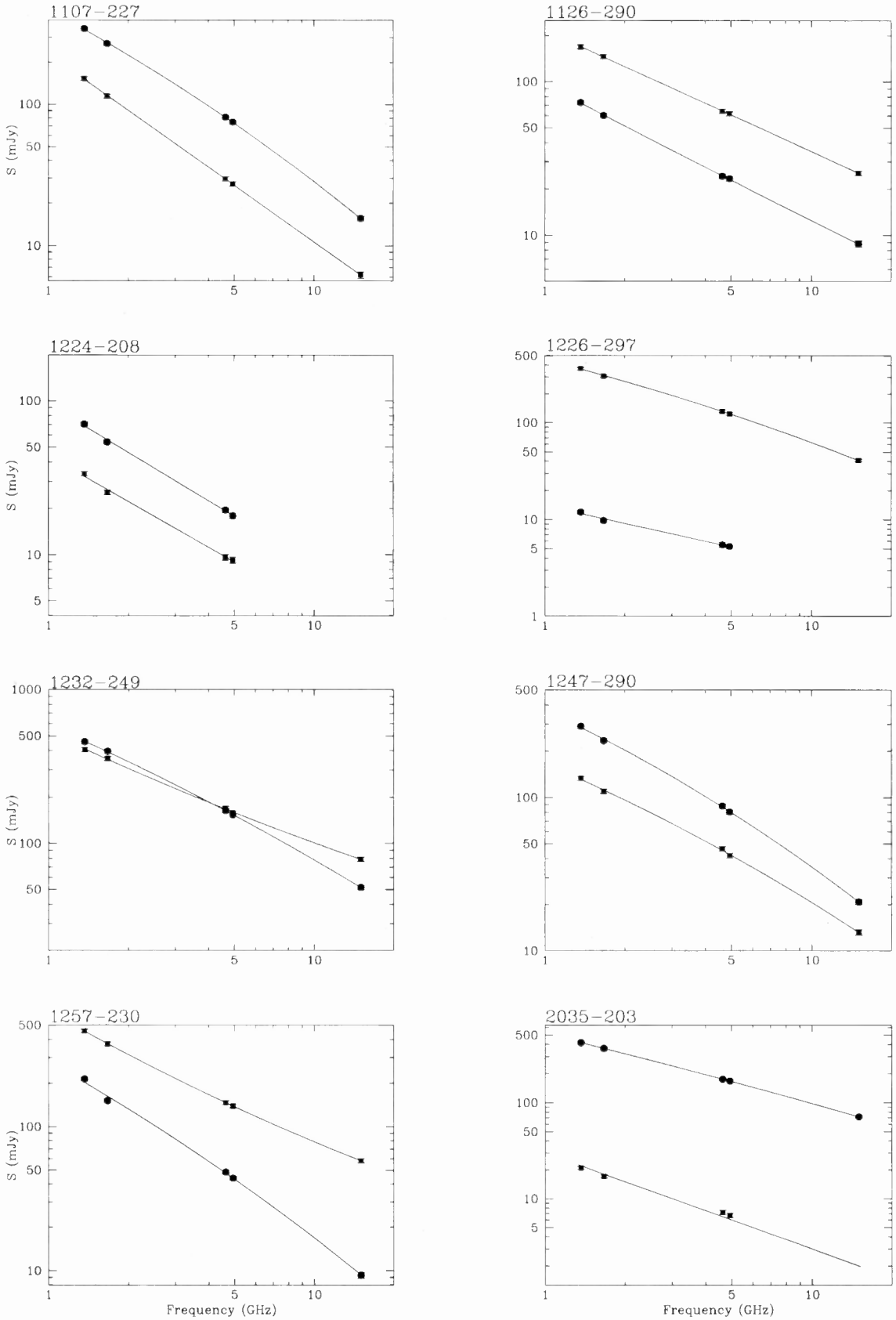

Figure 4A.1 — *continued*

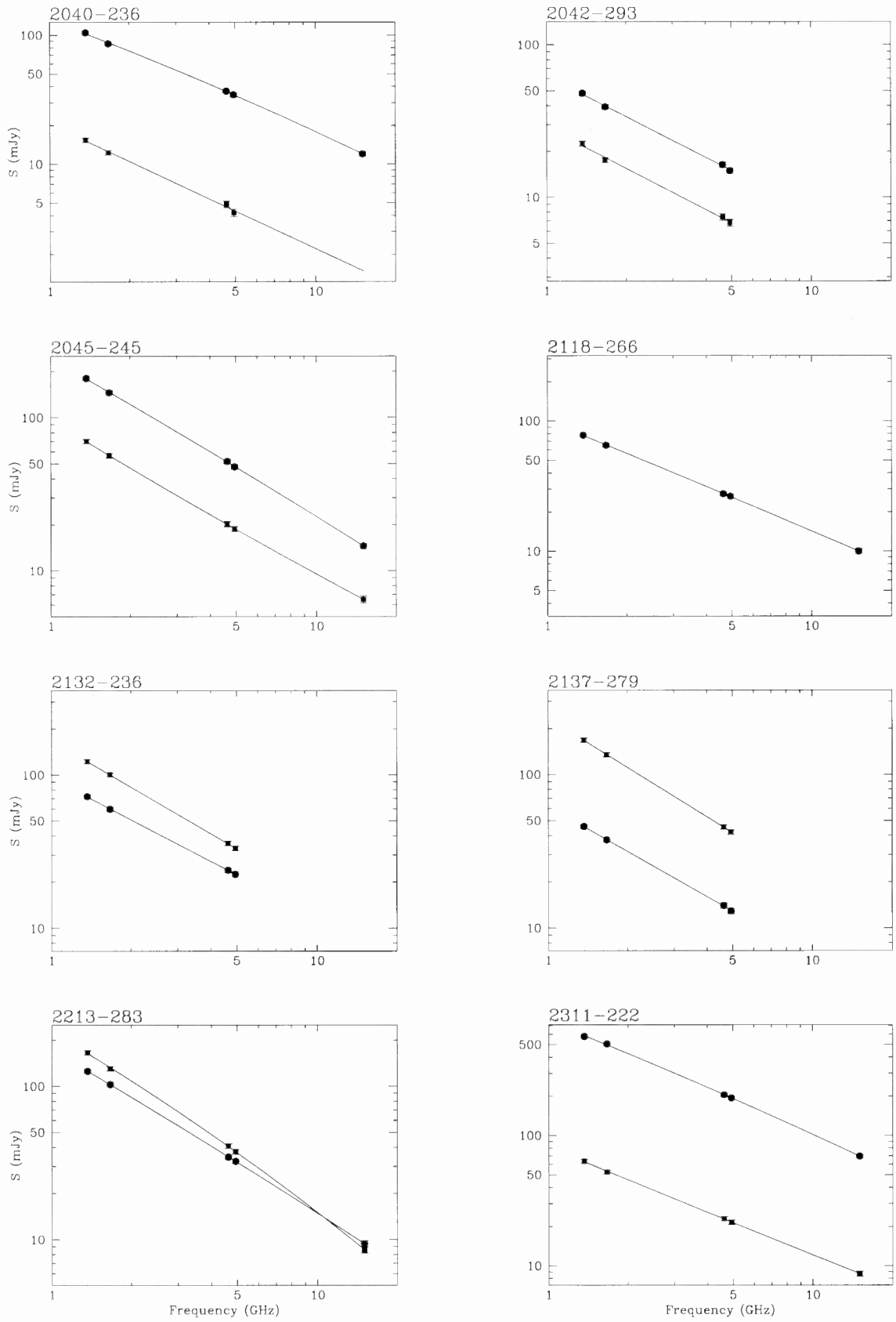

Figure 4A.1 — *continued*

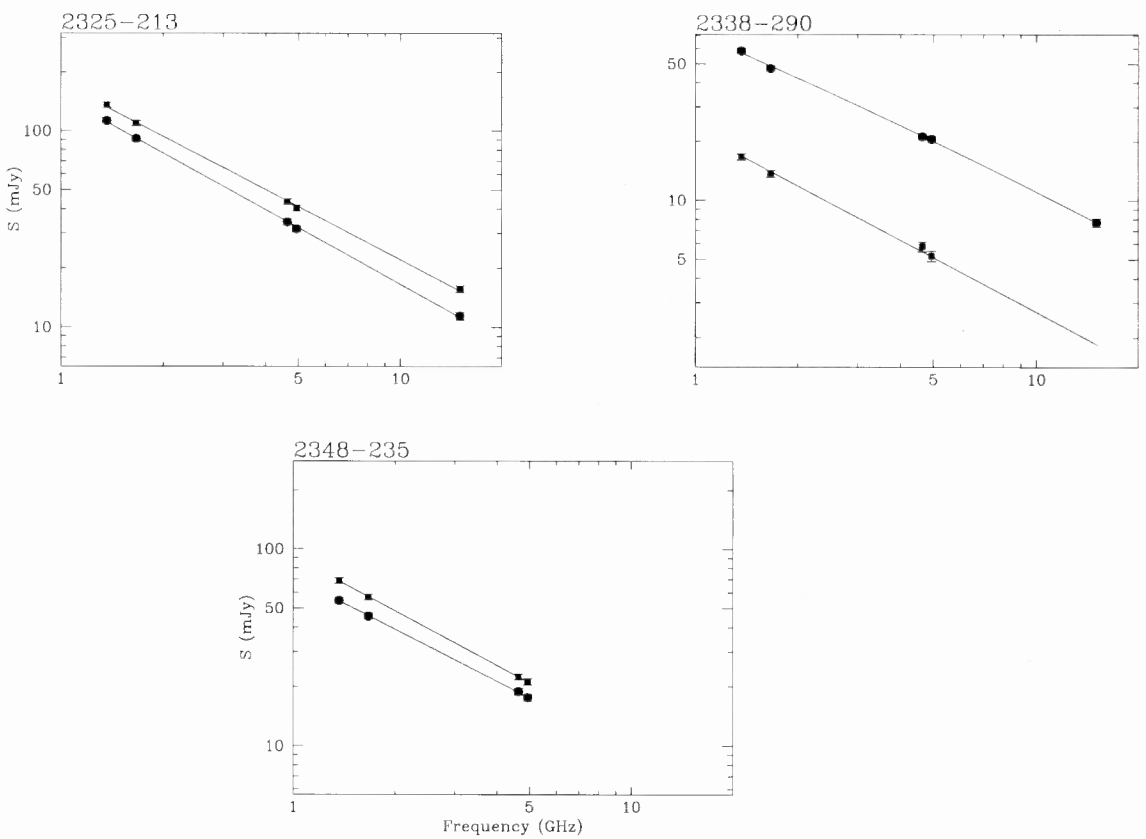

Figure 4A.1 – *continued*

Table 4A.1. The two point hotspot spectral indices between L and C bands, and C and U bands.

Source	z	α_C^L	α_U^C	Source	z	α_C^L	α_U^C
0017−207N	0.545	0.984	1.000	1052−272N	1.103	1.117	1.422
0017−207S	0.545	0.899	0.884	1052−272S	1.103	0.986	0.756
0058−229N	0.706	0.763	0.937	1107−218E	1.5	0.866	–
0058−229S	0.706	0.712	0.794	1107−218W	1.5	0.789	–
0133−266N	1.53	0.910	–	1107−227N	2.0	1.186	1.406
0133−266S	1.53	1.078	–	1107−227S	2.0	1.333	1.331
0137−263N	1.1	0.812	–	1126−290N	0.41	0.891	0.868
0137−263S	1.1	0.943	–	1126−290S	0.41	0.792	0.795
0148−297N	0.41	0.836	0.665	1224−208N	1.5	1.04	–
0148−297S	0.41	0.875	0.821	1224−208S	1.5	0.988	–
0325−260N	0.638	0.880	–	1226−297S	0.749	0.837	0.995
0325−260S	0.638	0.910	–	1232−249N	0.352	0.857	0.979
0346−297S	0.413	0.913	–	1232−249S	0.352	0.733	0.638
0428−281E	0.65	0.973	1.180	1247−290N	0.770	0.981	1.220
0428−281W	0.65	0.920	1.144	1247−290S	0.770	0.877	1.055
0437−244N	0.840	0.905	0.845	1257−230N	1.109	1.185	1.403
0437−244S	0.840	0.854	–	1257−230S	1.109	0.919	0.787
0454−220N	0.533	0.917	0.955	2035−203E	0.516	0.710	0.766
0454−220S	0.533	1.045	0.931	2035−203W	0.516	0.874	–
0551−226N	0.8	0.796	–	2040−236E	0.704	0.847	0.955
0551−226S	0.8	0.879	–	2040−236W	0.704	0.966	–
0937−250N	0.9	0.933	–	2042−293N	1.9	0.892	–
0937−250S	0.9	1.000	–	2042−293S	1.9	0.897	–
0938−205N	0.371	0.792	–	2045−245N	0.73	1.024	1.079
0938−205S	0.371	0.710	–	2045−245S	0.73	1.016	0.961
0947−249N	0.854	1.091	1.13	2118−266E	0.343	0.840	0.868
0947−249S	0.854	1.018	0.92	2132−235N	0.81	0.903	–
0955−283E	0.8	0.895	–	2132−235S	0.81	1.012	–
0955−283W	0.8	0.951	–	2137−279N	0.64	0.976	–
1022−250N	0.34	0.805	–	2137−279S	0.64	1.072	–
1022−250S	0.34	0.913	–	2213−283E	0.946	1.057	1.112
1023−226N	0.586	0.816	–	2213−283W	0.946	1.151	1.324
1023−226S	0.586	0.836	–	2311−222E	0.434	0.861	0.923
1025−229N	0.309	0.899	–	2311−222W	0.434	0.827	0.823
1025−229S	0.309	0.915	–	2325−213E	0.58	0.976	0.929
1026−202N	0.566	0.870	0.939	2325−213W	0.58	0.927	0.866
1026−202S	0.566	0.874	0.783	2338−290N	0.446	0.802	0.873
1029−233N	0.611	0.858	–	2338−290S	0.446	0.881	–
1029−233S	0.611	0.856	–	2348−235N	0.952	0.873	–
				2348−235S	0.952	0.916	–

4B. X-band images

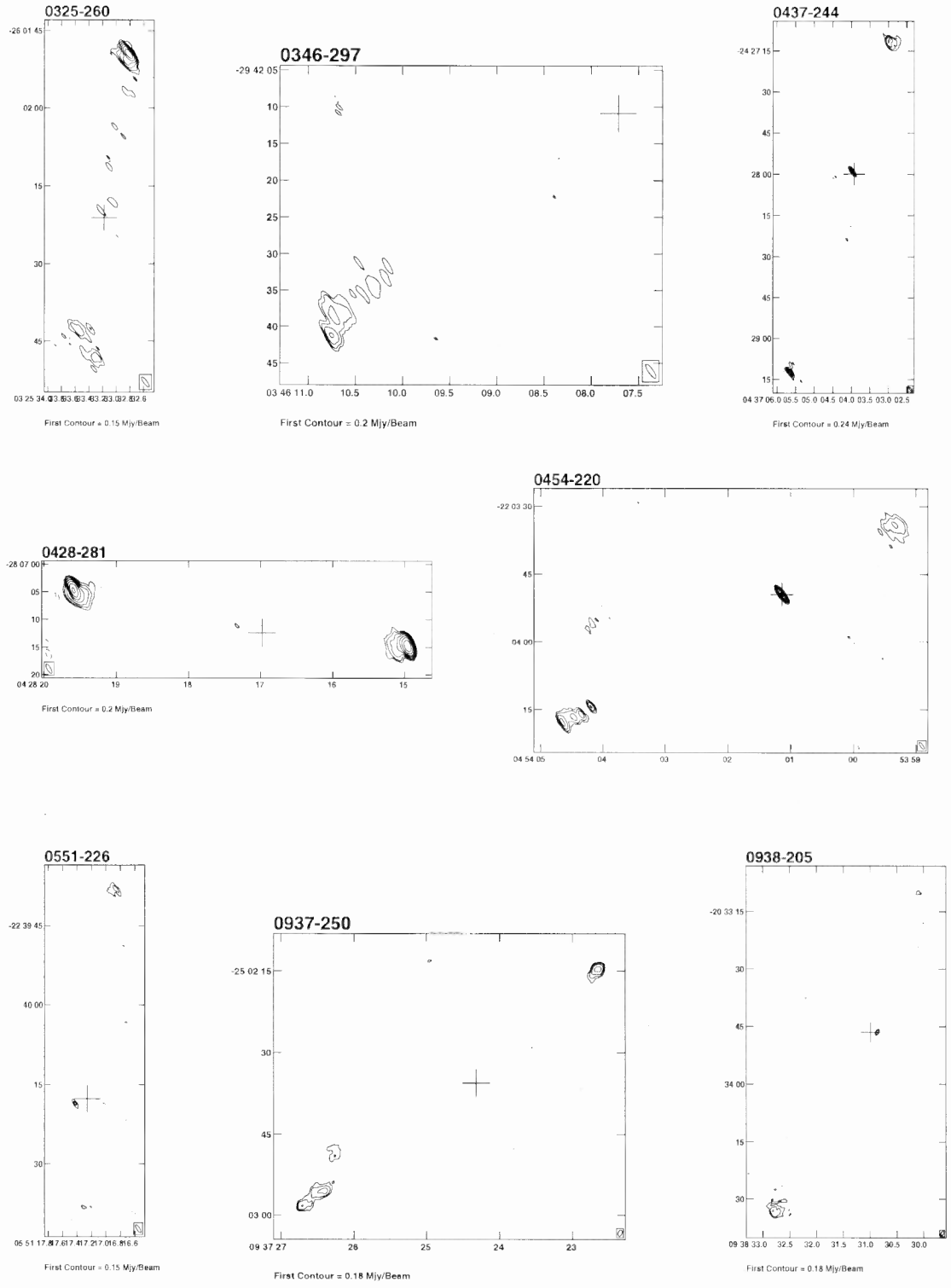

Figure 4B.1 Images of the sample of sources at X Band (8 GHz). The contour levels are -2, -1, 1, 2, 4, 8, 16, 32, 64, 128, 256, 512 mJy/beam times the base level given below each figure. X axis is right ascension and Y axis is declination in B1950 co ordinates.

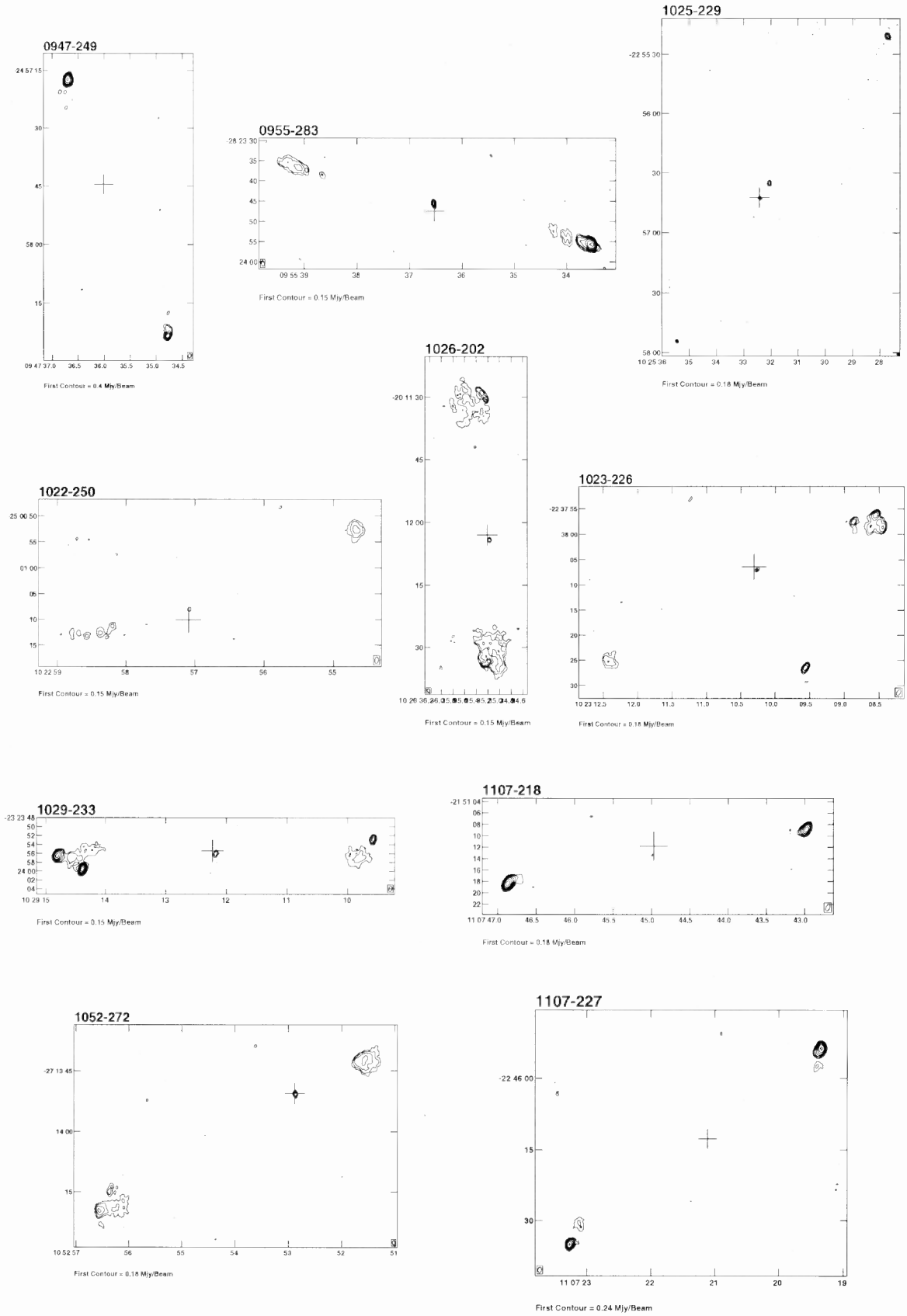

Figure 4B.1 – *continued*

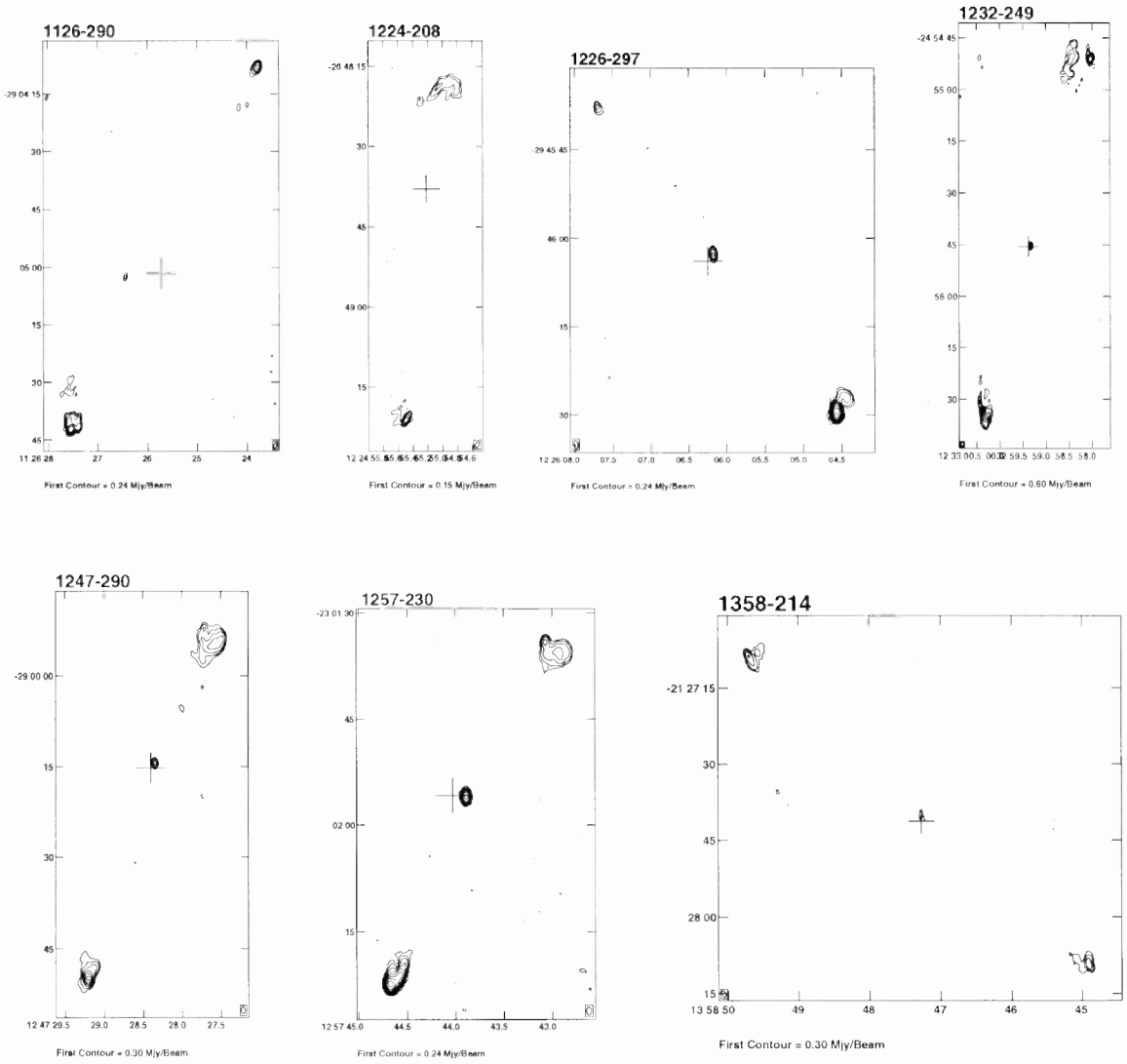

Figure 4B.1 – *continued*

4C. U-band images

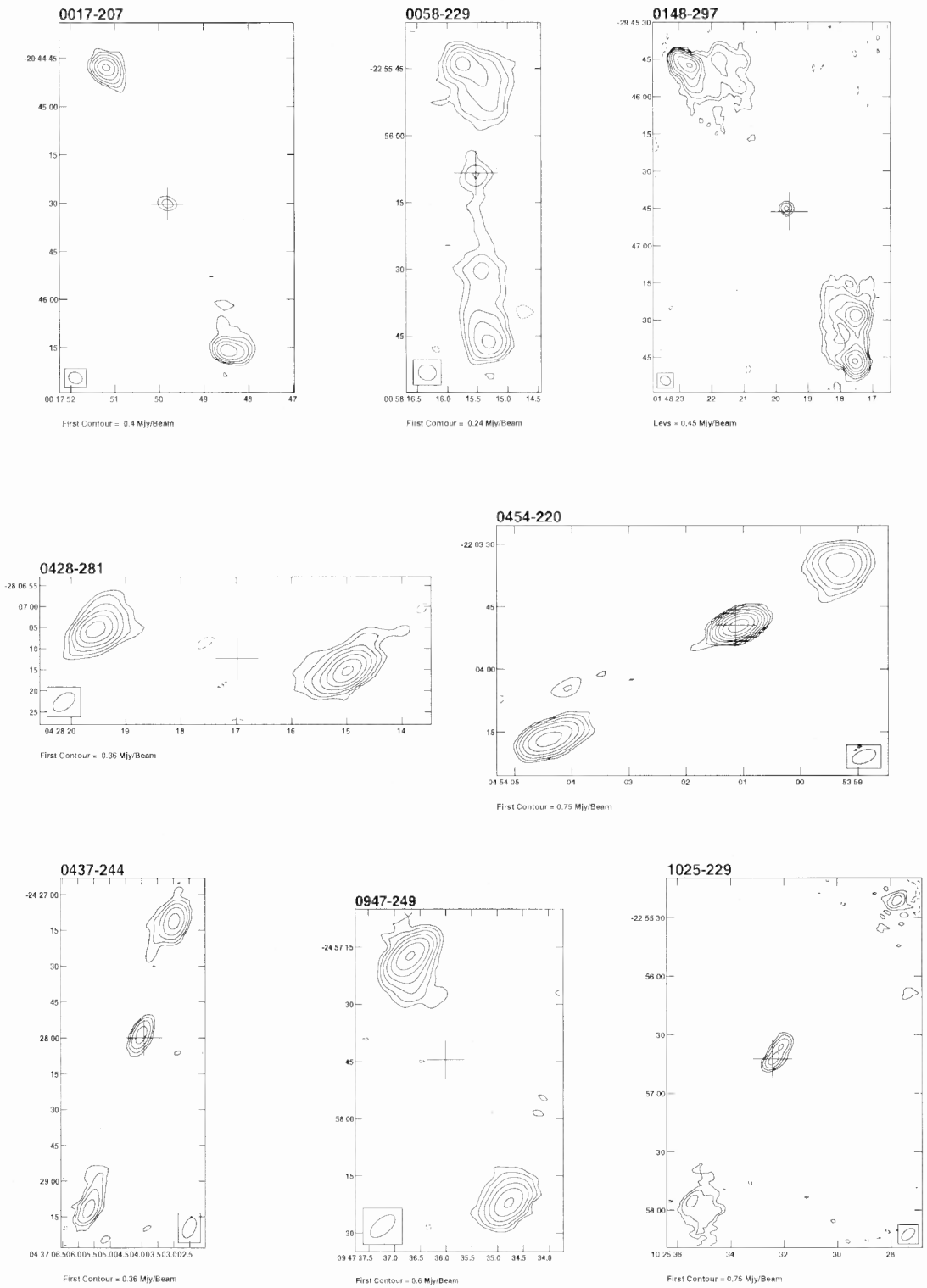

Figure 4C.1 Images of the sample of sources at U Band (15GHz). The contour levels are -2, -1, 1, 2, 4, 8, 16, 32, 64, 128, 256, 512 mJy/beam times the base level given below each figure. The X axis is right ascension and Y axis is declination in B1950 co-ordinates.

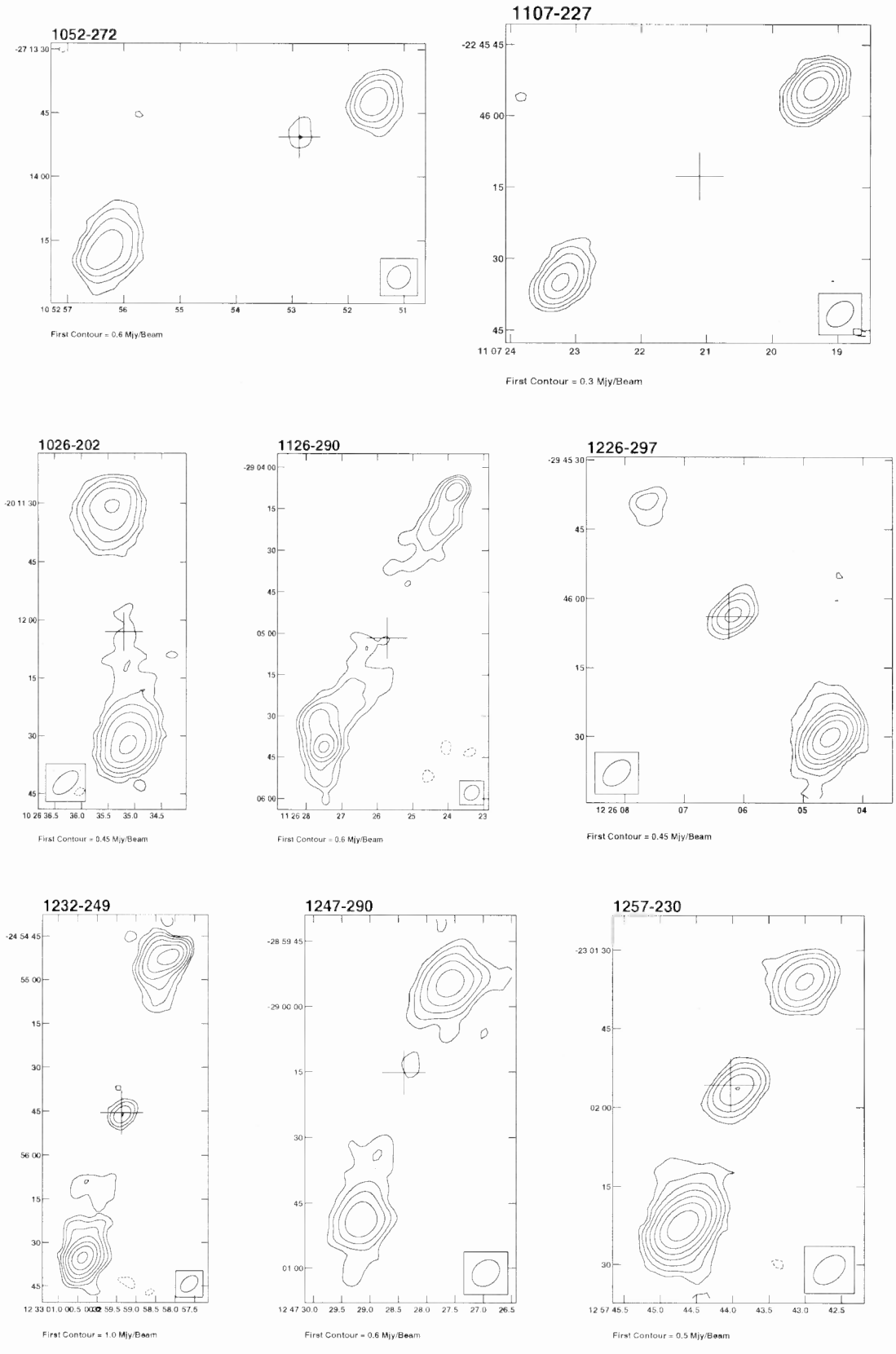

Figure 4C.1 – *continued*

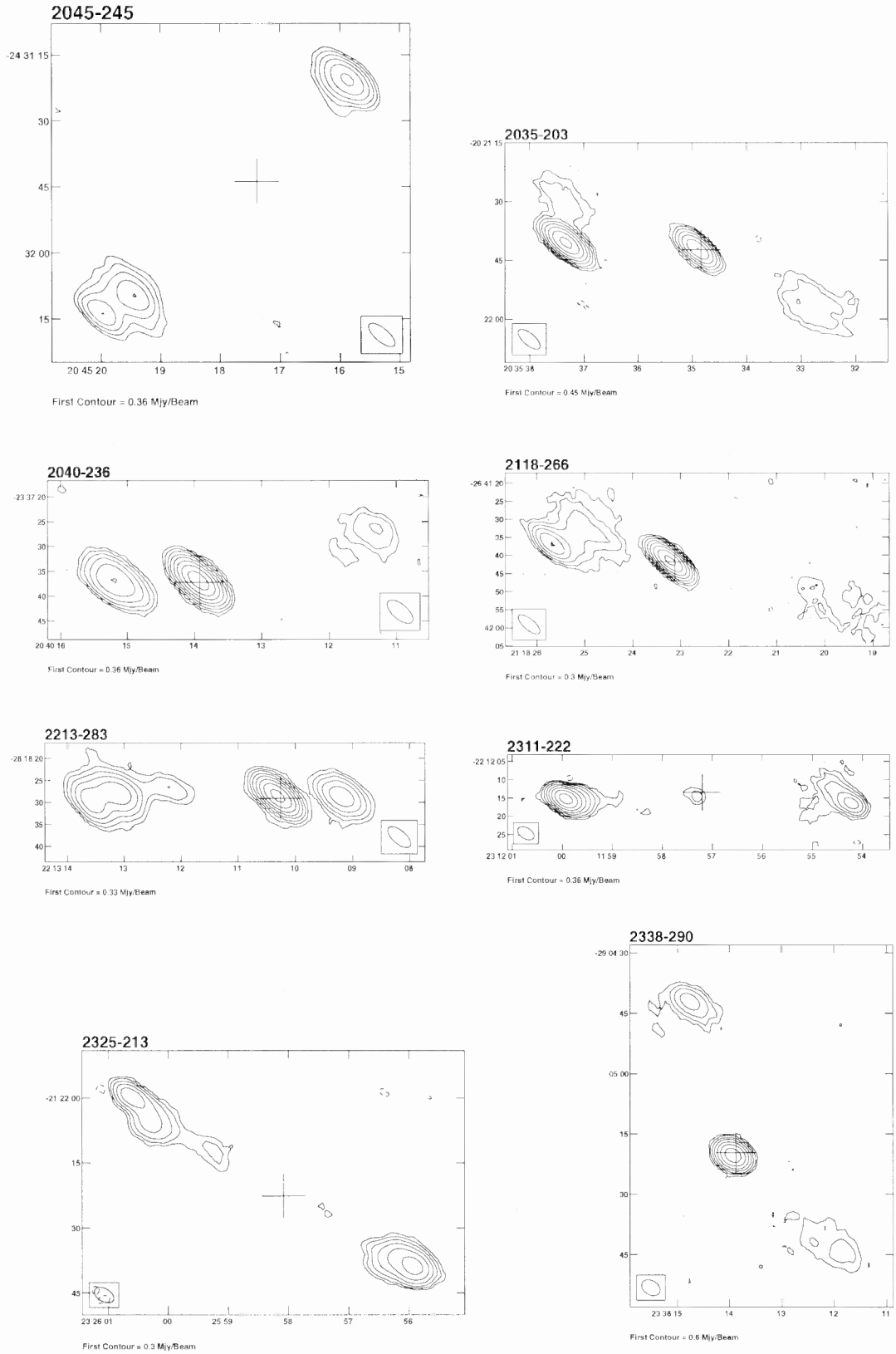

Figure 4C.1 – *continued*